BIOPHYSICS

Force production of human cytoplasmic dynein is limited by its processivity

Sibylle Brenner[1]*, Florian Berger[2], Lu Rao[1], Matthew P. Nicholas[1,3†], Arne Gennerich[1,2‡]

Cytoplasmic dynein is a highly complex motor protein that generates forces toward the minus end of microtubules. Using optical tweezers, we demonstrate that the low processivity (ability to take multiple steps before dissociating) of human dynein limits its force generation due to premature microtubule dissociation. Using a high trap stiffness whereby the motor achieves greater force per step, we reveal that the motor's true maximal force ("stall force") is ~2 pN. Furthermore, an average force versus trap stiffness plot yields a hyperbolic curve that plateaus at the stall force. We derive an analytical equation that accurately describes this curve, predicting both stall force and zero-load processivity. This theoretical model describes the behavior of a kinesin motor under low-processivity conditions. Our work clarifies the true stall force and processivity of human dynein and provides a new paradigm for understanding and analyzing molecular motor force generation for weakly processive motors.

INTRODUCTION

Cytoplasmic dynein 1 (hereafter referred to as dynein) is a large >1.5-MDa multiprotein complex (*1*). As a member of the AAA+ [adenosine triphosphatase (ATPase) associated with various cellular activities] protein family (*2*), mammalian dynein performs a multitude of cellular functions. These include minus end–directed microtubule (MT) transport of various cargos (*3*), mitosis (*4*), nuclear positioning (*5*), and cell migration (*6*). The dynein holoenzyme is a dimer of heavy chains (HCs); these comprise the ring-shaped motor domain (MD; containing six AAA+ domains), the MT-binding stalk, and the dimerization domain (tail) (*7*). The latter forms a scaffold for associated subunits, such as light chains (LCs), light intermediate chains (LICs), and intermediate chains (ICs), as well as for regulatory cofactors, such as dynactin, Lis1 (lissencephaly protein 1), NudE (nuclear distribution factor E), and NudEL (NudE-like protein) (*1*).

In this work, we sought to clarify longstanding uncertainties regarding mammalian dynein's single-molecule, intrinsic stall force (maximal sustained force generation in the absence of cofactors) and processivity (ability to take multiple steps before MT dissociation, as measured by run length). Over the past several decades, dynein's molecular function has been investigated both in vivo and in vitro. Until recently, most studies have focused on dyneins from *Dictyostelium discoideum* and *Saccharomyces cerevisiae* (yeast) due to their stability, ease of genetic manipulation, and established purification protocols (*8*, *9*). However, there are notable differences between the function of yeast dynein and that of higher eukaryotes (*10*). Even in the absence of cofactors, yeast dynein is highly processive. The run length of isolated yeast dynein is in the range of 1 to 3 μm (*8*, *11*), with a measured stall force of ~4 pN (*12*, *13*) [we show here that the previously reported 7-pN stall force (*14*) is likely the result of an unintended electronic low-pass filtering of the trapping data; see Supplementary Materials]. In contrast, the study of mammalian dynein has yielded variable results. A wide range of single-molecule stall forces, between ~0.8 and 7 pN (*15*–*21*), have been reported, and single-molecule processivity has ranged from immeasurable (*22*, *23*), to over several hundred nanometers (*17*), to 1 μm (*20*, *24*, *25*). A number of technical issues have likely contributed to the variability of both processivity and stall force measurements for mammalian dynein. These include variations in protein purification, protein labeling, and microscopy techniques. We discuss these issues in detail below, but much of the challenge in these measurements actually arises from the relatively low intrinsic processivity of mammalian dynein. Whereas yeast dynein frequently achieves its stall force before MT dissociation (as determined by a plateau or "stalling" of its displacement versus time) (*14*), mammalian dynein's low processivity results more frequently in short displacements with runs terminated by detachment from the MT rather than sustained force plateaus (*17*, *26*). Do the forces achieved represent stall force or simply "premature" MT dissociation due to low processivity? How can stalling be defined objectively? Is processivity affected by force? Answering these questions in the absence of dynein cofactors has been challenging but important for at least two reasons. First, there are reports of dynactin-independent recruitment of dynein to organelles (*27*, *28*), and understanding dynein function under these circumstances will be greatly aided by accurately characterizing its single-molecule processivity and force generation in isolation. Second, it is essential to study dynein function in isolation to understand the effects of its various cofactors. Despite variable processivity in vitro (see further discussion below), mammalian dynein complexes have been shown to move over several micrometers in vivo (*17*, *18*, *29*). However, this appears to be mediated by the presence of dynactin and other cofactors.

Recent publications have shown that when mammalian dynein is complexed with dynactin via the coiled coil–containing cargo adaptor, Bicaudal-D2 (BicD2), dynein moves over several micrometers in vitro [~5 (*30*) and ~9 μm (*31*)]. This augmented processivity appears to result from relief of a low MT-affinity, autoinhibited "phi-particle" (*32*) conformation [in which the stalks cross each other (*7*, *26*)] by dynactin and BicD (as well as other coiled coil–containing cargo adaptors) (*7*). Cofactor binding reorients the two

[1]Department of Anatomy and Structural Biology and Gruss Lipper Biophotonics Center, Albert Einstein College of Medicine, Bronx, NY 10461, USA. [2]Laboratory of Sensory Neuroscience, The Rockefeller University, New York, NY 10065, USA. [3]Medical Scientist Training Program, Albert Einstein College of Medicine, Bronx, NY 10461, USA.
*Present address: Grace Church School, New York, NY 10003, USA.
†Present address: Flaum Eye Institute, University of Rochester Medical Center, NY 14642, USA.
‡Corresponding author. Email: arne.gennerich@einstein.yu.edu

MDs parallel to each other and converts mammalian dynein from a weakly processive (*10*) to an ultraprocessive motor (*30*, *31*, *33*). It is likely that, by virtue of increased processivity, these dynein-dynactin-BicD2 complexes exhibit more classic stalling behavior and greater stall forces in optic tweezers assays (*12*, *34*). However, without knowing dynein's intrinsic function, it is impossible to understand the effects of its cofactors on force generation. Is the stall force actually increased or is it the same but simply easier to observe? Might cofactor association increase processivity while actually reducing stall force? Moreover, although dynein appears to be more processive when bound by these cofactors, its intrinsic processivity is still somewhat uncertain (*10*, *22*). We clarify several of these questions here by observing both processivity and force generation in an optic tweezers assay and developing a theoretical model to describe these observations and predict both intrinsic processivity and stall force despite the difficulty of observing these attributes directly. Below, we discuss some of the technical challenges in measuring mammalian dynein single-molecule function.

Different purification strategies and protein sources [brain (*16*, *17*, *20*, *23*, *25*) and tissue culture (*26*, *35*)] may have resulted in varying fractions of inactive or conformationally inhibited proteins [see, e.g., (*30*, *31*)]. In addition, when determining dynein processivity using optical microscopy (using attachment to fluorescence tags or visible beads to track the motor), the detection limit is typically several hundred nanometers. Therefore, run lengths for single motors have remained immeasurable in some studies (*22*, *23*). In contrast, others have reported a run length of 1.3 μm for 1% of the cofactor-free dynein molecules (*30*). When bound to beads, mammalian dynein generates movement over ~0.7 to 1 μm (*20*, *24*, *36*). Conversely, using both Qdots suited for high-precision fluorescence microscopy and bead assays, Ori-McKenney *et al.* (*17*) measured a run length of ~0.3 μm for a subfraction of the motor population. In addition to a low fraction of moving motors, diffusive bidirectional events have also often been reported instead of, or in addition to, unidirectional movement (*17*, *20*, *22*, *23*, *25*). A recent study by Torisawa *et al.* (*26*) reported bidirectional diffusion biased toward the MT minus end, with an average run length of ~100 nm. In this case, it was attributed to an autoinhibited conformation of dynein dimers in the absence of cofactors. However, even in the presence of dynactin/BicD2, the diffusive fraction can constitute ~30% of all data (*30*).

In the present study, we analyze native human dynein purified from human embryonic kidney (HEK) 293 cells (*37*, *38*) using single-molecule optical tweezers. With this method, we confirm a very low fraction of stalling events (≥200 ms), similar to other studies (*17*), which complicates stall force analysis. On the basis of the reported submicroscopic run length of mammalian dynein (*10*), we hypothesized that the ability to observe motor stalling is directly limited by the motor's weak processivity. That is, dynein force generation is commonly observed at trap stiffnesses of 0.01 to 0.02 pN/nm, resulting in the motor having to travel 50 to 100 nm to reach a force of 1 pN. Our analysis, which included a range of trap stiffnesses, indeed reveals a novel hyperbolic trap stiffness dependence for the average detachment forces, with a force plateau of ~2 pN at saturating adenosine triphosphate (ATP) concentrations. This force plateau coincides with the measured stall force at high trap stiffnesses. We further derive a theoretical model that accurately describes the hyperbolic trap stiffness dependence and the experimentally measured force plateau. This equation is independent of motor compliance and allows for determination of the maximal force generation of dynein without the observation of motor stalling. We also find that a hyperbolic increase in measured forces correlates with a hyperbolic decrease in the corresponding distance displacements. Dynein's run length at zero load can therefore be estimated from the *y* intercept at a trap stiffness of zero, resulting in a zero-load run length of ~100 nm. Application of our experimental framework to full-length yeast dynein and kinesin-1, both of which are highly processive motors, reveals that, at low ionic strength, both motors are insensitive to changes within a practical trap stiffness range, while a similar trap stiffness dependence is observed for kinesin-1 at elevated ionic strengths. Our study, therefore, provides a method for determining the force-free processivity and stall force of mammalian dynein (and possibly other cytoskeletal motors), without the need to directly measure dynein displacements at zero load or to directly measure motor stalling. Thus, our work clarifies longstanding discrepancies regarding mammalian dynein single-molecule functional properties and provides a novel framework for studying weakly processive molecular motors in general.

RESULTS

Processivity and force generation of individual native human dynein complexes

To determine the motion and force generation capabilities of human dynein, we used a native human dynein containing a multifunctional streptavidin- and green fluorescent protein (GFP)–tagged intermediate chain (mfGFP-IC) (*37*, *38*). Tagged dynein complexes were purified from HEK293 cells using the streptavidin tag in the mfGFP-IC construct via one-step StrepTrap column purification (fig. S1A). This yielded mostly dynein HC dimers, as confirmed by blue native polyacrylamide gel electrophoresis (BN-PAGE; fig. S1B). Western blot analysis further confirmed the copurification of dynein subunits (IC, LC, and LIC) and showed trace amounts of cofactors, including Lis1, nuclear distribution element 1 (Nde1), and dynactin p150 subunit (fig. S1C). To remove inactive motors, bound cofactors, dynein aggregates, and other possible contaminants, we then conducted a second purification step using the MT-binding and release (MTBR) assay. Here, dynein was bound to MTs in the presence of the ATP analog, AMP-PNP (adenylyl-imidodiphosphate). Active motors were then released by the addition of ATP and salt (fig. S1D). After MTBR, cofactors were no longer detectable by Western blot, and when adhered to carboxyl-trapping beads, the purified dynein complex exhibited exclusively minus end–directed motility (see Supplementary Materials for additional information about the characterization of the StrepTrap- and MTBR-purified protein fractions).

To next test whether native human dynein is a weakly processive motor in isolation, we conducted optical trapping studies (Fig. 1, A and B). For these analyses, dynein was adhered to 1-μm-diameter carboxyl beads, and processive motion was measured by determining the motile bead fraction as a function of relative motor bead concentration (Fig. 1C). In contrast to single-molecule fluorescence microscopy and MT-landing rate assays that have a resolution limit of several hundred nanometers (*22*, *30*, *31*), bead displacements in the sub-100-nm range can be resolved in the optical trap (Fig. 1B). Because most publications on mammalian dyneins [see, e.g., (*15*, *17*, *18*, *20*, *21*)] have reported stall forces between 1 and 2 pN, we chose a trap stiffness of k = 0.01 pN/nm, which is expected to result in bead-trap

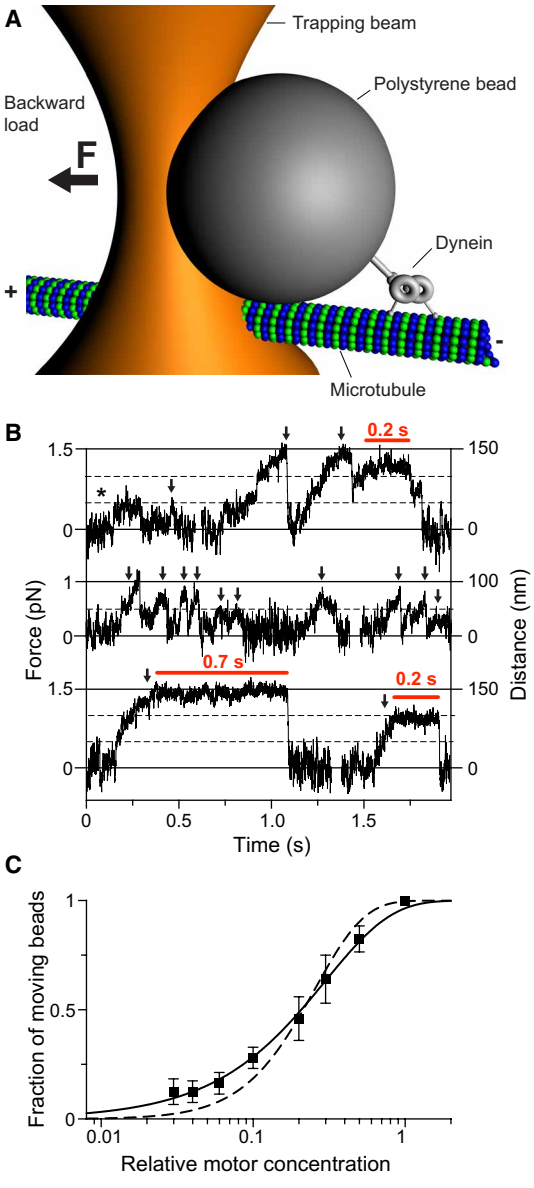

Fig. 1. Optical trapping assay to probe dynein force generation. (**A**) Schematic of the optical tweezers assay (not to scale). A 0.9-μm-diameter carboxyl bead is nonspecifically bound to a purified single human dynein and is trapped by a near-infrared optical trapping beam focused via a high numerical aperture microscope objective lens. The trap holds the bead directly above an MT that is covalently linked to the glass surface of the coverslip. When the dynein binds to and moves along the MT in the presence of ATP, it pulls the attached bead with it. The trap resists this motion, exerting a force $F = -k \times \Delta x$ on the bead-motor complex, where k is the trap stiffness and Δx is the distance from the trap center to the center of the bead. (**B**) Example traces at 1 mM ATP and $k = 0.01$ pN/nm (see also fig. S2B). Stalling events (red horizontal bars) can be observed but are rare. Fast events, including large single forward-backward steps without any resolved intermediate steps (black star), are frequent. Events that are counted as force generation events are marked with black arrows. (**C**) Dilution curve counting beads as moving if forces equaled or exceeded 0.5 pN. Error bars were calculated assuming a binomial distribution. Twelve to 85 beads were tested for each dilution ($N_{total} = 318$). The curves are fits to equations assuming processive motors (Eq. 6, $\lambda = 3.3 \pm 0.1$, solid line, $R^2 = 0.996$) and nonprocessive motors (Eq. 7, $\lambda = 7.9 \pm 0.7$, dashed line, $R^2 = 0.949$).

separations of 100 to 200 nm. A bead was counted as moving if its displacement was ≥50 nm, equivalent to ≥0.5 pN. The dilution curve obtained from this assay was then analyzed on the basis of two models [see Materials and Methods, Supplementary Materials, and (*39*–*41*)]: one describing force generation by one or more motors ("processive" model) and the other describing force generation driven by two or more motors ("nonprocessive" model). We found that our data were best described by the processive model [R^2 = 0.996; Akaike's information criterion (AIC) probability of 99.99%]. This was true even when beads displaying exclusively large (up to 50 nm) single forward-backward steps, without any resolved intermediate steps (Fig. 1B), were counted as nonmoving (R^2 = 0.992; AIC probability of 99.97%; fig. S2A) [we suspect that these displacements are generated by dynein motors that transition reversibly from the autoinhibitory to the open conformation (*7*)]. We, therefore, find that under these experimental conditions, native human dynein is a weakly processive motor (*17*).

The "stall force" of single human dynein complexes at saturating [ATP] was next determined by analyzing trapping data obtained at the single-molecule level [in this case, ≤30% bead motility (*39*–*41*)]. Stalling was defined as a ≥ 200-ms force plateau [as in (*17*)], excluding jump-like events to such a plateau (Fig. 1B). The resulting stall force histogram (Fig. 2A) followed a Gaussian distribution, with an average of 0.9 ± 0.3 pN (±SD; N = 77; k = 0.01 pN/nm), which is consistent with previously published stall forces for mammalian dyneins (*15*, *17*, *18*, *20*, *21*). However, the vast majority of runs did not result in stalling, and in most cases, dynein released prematurely from the MT (Fig. 1B, middle). Hence, the stall percentage (number of stalling events/number of all events × 100%) was extremely low (6.8%). In addition, the detachment force, defined as the average maximum force of all events, was found to be significantly lower (0.63 ± 0.01 pN, ±SEM) than the stall force (0.89 ± 0.02 pN, ±SEM) (Fig. 2, A and B). It has been previously noted (*42*) that motors with low processivity, such as kinesin-5 (Eg5), rarely show clear stalling events before dissociation. Our observations therefore suggest that the limited processivity of human dynein in isolation may limit the observed stall force in the optical tweezers assay.

Processivity limits the measured peak force of isolated human dynein

To determine whether dynein's weak processivity did decrease its measured force generation, we repeated the optical trapping experiments at a trap stiffness of 0.03 pN/nm (such that dynein has to move only ~33 nm to reach a force of 1 pN). As expected, both the stall forces (Fig. 2A) and the detachment forces (Fig. 2B) increased with elevated trap stiffness (for all presented detachment force analyses, we took all events into account that were identifiable as force generation events, even when they occurred below 0.5 pN). Next, we raised the trap stiffness to 0.03 pN/nm for a given dynein-bound bead, following data acquisition at 0.01 pN/nm, to show that individual motors exhibiting one force generation behavior at a lower trap stiffness exhibit larger peak forces at higher trap stiffness. As expected, we found that force output increased as the trap stiffness was raised (Fig. 2C). We then determined whether the increased force generation at higher trap stiffnesses is reversible or whether dynein switches into a persistent high-force state, even if the trap stiffness is reduced again. To distinguish between these possibilities, we changed the trap stiffness from 0.06 to 0.01 pN/nm and back to

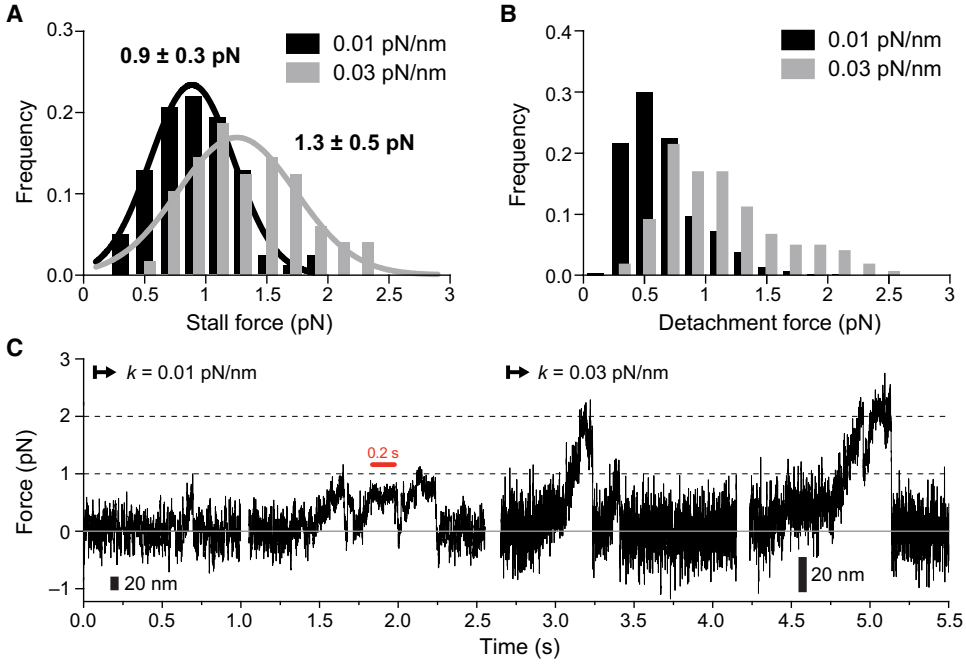

Fig. 2. Force generation of human dynein increases with increasing trap stiffness. (**A**) Stall force histograms of StrepTrap-purified and MT-binding released human dynein counting stalling events ≥200 ms and excluding jump-like behavior measured at $k = 0.01$ pN/nm (black bars) and $k = 0.03$ pN/nm (gray bars). The Gaussian distributions (solid curves) are centered at 0.9 ± 0.3 pN (±SD; $N = 77$) and 1.3 ± 0.5 pN (±SD; $N = 48$). (**B**) All measured forces ("detachment forces") acquired at $k = 0.01$ pN/nm (mean force: 0.64 pN; $N = 572$) and $k = 0.03$ pN/nm (mean force: 1.1 pN; $N = 225$). (**C**) Example record showing force generation events of a single dynein molecule bound to trapping bead measured at 0.01 pN/nm (left) and subsequently at 0.03 pN/nm (right), demonstrating an increase in force generation with increasing trap stiffness.

0.06 pN/nm (fig. S3). From these experiments, we found that the trap stiffness–induced increase in measured force generation is reproducible.

To determine dynein's maximal force-generating capabilities, the impact of its weak processivity must be negligible. Therefore, we adjusted the trap stiffness over a wide range of values (0.005 to 0.1 pN/nm), thereby probing the effects of run length on the measured forces. The force histograms obtained at 0.01 and 0.02 pN/nm (Fig. 2B and fig. S4) are in the range of previously reported values (*15*, *17*, *18*, *20*, *21*, *26*). In addition, the obtained mean detachment forces are statistically indistinguishable from the mean detachment forces measured at the same trap stiffnesses for dynein motors that are attached specifically to the beads coated with anti-GFP antibodies against the GFP-tagged IC of dynein ($P < 0.97$ at 0.01 pN/nm and $P < 0.83$ at 0.02 pN/nm for nonspecific versus specific bead coupling; fig. S4), demonstrating that the measured detachment forces do not depend on the coupling strategy. When plotting the cumulative distribution functions (CDFs) of the detachment forces measured at low to high trap stiffnesses (Fig. 3A), a continuous increase in force was observed, a phenomenon that has, to our knowledge, not been reported previously. In contrast, the CDFs of the detachment distances (Fig. 3B) showed a continuous decrease with increasing trap stiffness, consistent with the trend observed for the three initially tested trap stiffnesses of 0.01, 0.02, and 0.03 pN/nm. This dependence on trap stiffness for both the average detachment force and displacement distance appears to follow a hyperbolic function (Fig. 3C), with the forces approaching a force plateau at infinite trap stiffness and the distances decaying to zero. We, therefore, hypothesized that this detachment force plateau corresponds to the maximal force that a single mammalian dynein motor can generate in isolation.

The average detachment force increases hyperbolically with trap stiffness

To test our hypothesis that the average detachment force increases hyperbolically as a function of the trap stiffness and that the force plateau corresponds to the maximal force that a dynein molecule can generate in isolation, we derived an analytical equation for the average detachment force. In this model, the average detachment force is defined as follows

$$\langle F \rangle = \int_0^{F_s} F p(F)\, dF \tag{1}$$

where F_s is the stall force, and $p(F)$ is the probability density of the detachment forces. This probability density is related to the motor's force-dependent unbinding rate ε, its force-velocity relation $v(F)$, and its compliance (*43*); here, the force-dependent stepping behavior of dynein's two MDs (*44*–*46*) is effectively accounted for by $v(F)$. However, because we record the trajectory of the trapped bead and not the trajectory of the moving motor (the trajectories of the bead and motor would only coincide if the motor were noncompliant), we transformed these quantities into parameters that describe the motor-powered bead movement. We, therefore, derived the probability density function as follows

$$p(F) = \frac{\varepsilon(F)}{k v_b(F)} e^{-\int_0^F \frac{\varepsilon(F')}{k v_b(F')} dF'} \tag{2}$$

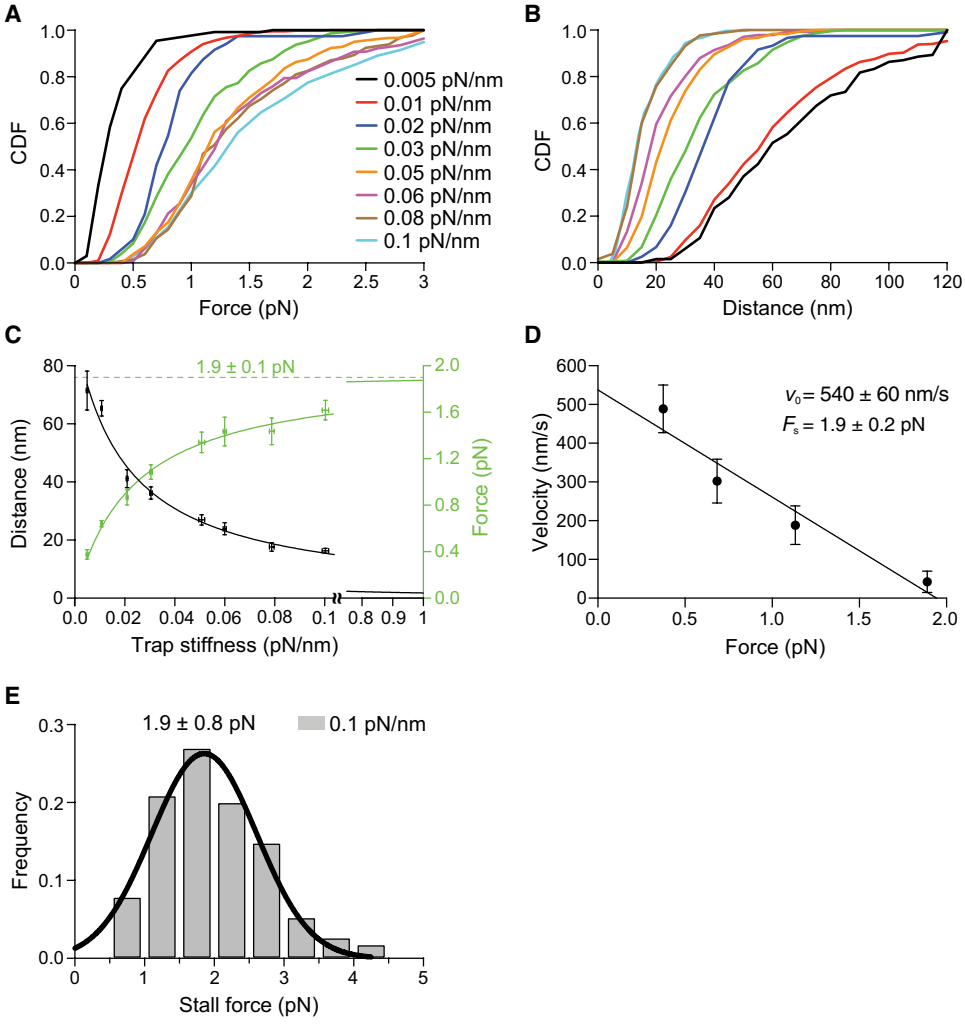

Fig. 3. Force production of human dynein is limited by its processivity. (**A** and **B**) CDFs of measured detachment forces (A) and corresponding displacements (B) acquired at various trap stiffnesses: black, $k = 0.005$ pN/nm; red, $k = 0.01$ pN/nm; blue, $k = 0.02$ pN/nm; green, $k = 0.03$ pN/nm; orange, $k = 0.05$ pN/nm; magenta, $k = 0.06$ pN/nm; brown, $k = 0.08$ pN/nm; cyan, 0.1 pN/nm. (**C**) Forces and distances as a function of trap stiffness [trap stiffnesses are displayed as mean ± 95% confidence intervals (CIs)]. The average distances (left *y* axis, black spheres) and average forces (right *y* axis, green spheres) (the error bars represent the 95% CI of the mean) were fit to Eqs. 5 and 4 (black curve, $R^2 = 0.983$; green curve, $R^2 = 0.991$), resulting in the force-free run length x_0 = 91 ± 5 nm (±SEM) and the stall force F_s depicted by the dashed line (mean ± SEM). (**D**) Velocity versus force. Points are means, and error bars span 95% CIs of the mean. The solid line is a linear fit that intercepts the ordinate at 540 nm/s (±60 nm/s, ±SEM) and the abscissa at 1.9 pN (±0.2 pN, ±SEM; $N = 83$ to 84 at each force; 335 events total). (**E**) Stall force histogram compiling stall forces (≥200 ms) at $k = 0.1$ pN/nm ($N = 115$; mean ± SD from Gaussian fit).

where $\varepsilon(F)$ is the force-dependent unbinding rate, k is the trap stiffness, and v_b (F) the force-velocity relation of the bead [as $\varepsilon(F)$, k, and $v_b(F)$ have the units 1/s, N/m, and m/s, $p(F)$ has the unit 1/N]. To derive an analytical solution, we made two assumptions. First, we presumed that the force-velocity relation of the bead decreases linearly with the force, such that

$$v_b = v_0(1 - F/F_s) \quad (3)$$

where v_0 is the force-free velocity. By extracting the force-velocity relation from the recorded traces, we indeed find that this equation describes the experimental force-velocity relation reasonably well (Fig. 3D). Our second assumption is a force-independent constant unbinding rate, $\varepsilon(F) = \varepsilon$. While this is a rather crude approximation, we find that the resulting analytical solution fits the data well (see below). As a further validation of our theoretical framework, we also investigated a scenario in which the unbinding rate depends exponentially on force and obtained very similar estimates for the stall force and the force-free run length (fig. S5). These results suggest that the stall force and the force-free run length are well constrained parameters, but that the accurate form of the force-dependent unbinding rate cannot be obtained using this approach (see Supplementary Materials for a detailed discussion). Therefore, the assumption of a constant unbinding rate is sufficient for our analysis, and together with the linear force-velocity relation for the bead, we can finally obtain an analytical equation describing the average detachment force

$$\langle F \rangle = \frac{F_s}{1 + \frac{F_s}{k\,x_0}} \quad (4)$$

where $x_0 = v_0/\varepsilon$ is the force-free run length. Fitting this equation to the experimental data, we obtain a value of 1.9 ± 0.1 pN (±SEM) for F_s and 87 ± 6 nm (±SE) for the force-free run length, x_0. If we restrict the fit to the data acquired at trap stiffnesses up to only 0.05 pN/nm, we obtain a very similar result (1.9 ± 0.1 pN and 85 ± 7 nm), demonstrating that this method yields reliable results even if we obtain data in a relatively narrow range of trap stiffnesses. In addition, at the limit for an increased trap stiffness, $<F> \rightarrow F_s$. Providing further support that this analytical equation describes the data well enough, we find that the resulting value for F_s coincides with both the stall force value resulting from the force-velocity analysis (1.9 ± 0.2 pN, ±SE; Fig. 3D) and with the stall forces (≥200 ms) measured at the largest trap stiffness of 0.1 pN/nm (1.9 ± 0.1 pN, ±SE; Fig. 3E). In contrast, stall forces measured below 0.04 pN/nm deviate significantly from the hyperbolic plateau (Fig. 2A), suggesting that the ≥200-ms force plateaus at low trap stiffnesses do not correspond to true stalling events.

Analogous to the hyperbolic relationship between the detachment force and the trap stiffness, the average detachment distance decays hyperbolically with increasing trap stiffness (Fig. 3, B and C). As is the case for the average detachment forces, the data can be fit to the theoretical average run length by the equation

$$\langle x \rangle = \langle F \rangle / k = \frac{x_0}{1 + \frac{k\,x_0}{F_s}} \quad (5)$$

At the limit for a decreasing trap stiffness, the average run length converges to the force-free run length, $\langle x \rangle \rightarrow x_0$.

Thus, our theoretical analysis shows that the average detachment force and the average run length depend hyperbolically on the trap stiffness. In addition, the force plateau corresponds to the stall force of the motor. This suggests that the detachment forces measured at commonly used trap stiffnesses (0.005 to 0.04 pN/nm) may be limited by dynein's processivity. We, therefore, hypothesized that this behavior should also be observed with highly processive motors under conditions where their processivity is significantly impaired. To test this possibility, we analyzed two other MT-associated molecular motors—the highly processive yeast dynein and the plus end–directed kinesin-1—as a function of the trap stiffness in buffers of varying ionic strength.

Force generation of yeast dynein is insensitive to changes within a practical trap stiffness range

Yeast cytoplasmic dynein is a highly processive molecular motor that displays run lengths between 1 and 3 μm, with some runs up to 20 μm (*8*, *11*, *47*), and stall forces reported as high as 7 pN (*14*) (see Supplementary Materials for a detailed theoretical analysis that suggests that the previously measured 7-pN stall force likely resulted from an unintended electronic low-pass filtering during data acquisition). We analyzed the forces generated by the full-length yeast dynein construct, VY97-GFP [a GFP-tagged full-length motor (*14*)], at trap stiffnesses between 0.03 and 0.05 pN/nm (Fig. 4). Analysis of trap stiffnesses below 0.03 pN/nm was not feasible due to the limited reach of our optical trap (<300 nm), as escape of the dynein-bound beads from the trap occurred at lower trap stiffnesses. In a buffer system containing 30 mM Hepes and 100 mM KAc (potassium acetate stock solution pH adjusted to 7.0; see Materials and Methods), we did not detect any significant effect of trap stiffness on force (Fig. 4B), and we obtained an average stall force of 4.5 ± 0.7 pN (±SD; Fig. 4C). This is in agreement with our recent work (*13*) but is somewhat smaller than the previously published value (*14*) for the same construct (see Supplementary Materials for discussion). Therefore, even in 100 mM KAc, yeast dynein is sufficiently processive for its run length to have no impact on the observed forces. These trap stiffness–independent results also serve as internal control to show that our trapping instrument was accurately calibrated and functioning as expected.

Force generation of kinesin-1 becomes sensitive to trap stiffness at high ionic strength

We next analyzed the plus end–directed motor kinesin-1 using the well-characterized construct, K560-GFP, a 560–amino acid–long, tail-truncated construct of human conventional kinesin-1, with a C-terminal F64L/S65T variant of GFP (*48*–*50*). Because this construct has been previously shown to display significant salt-dependent reductions in run length (*50*), we considered it to be an ideal candidate to test the relationship between processivity and force generation for a kinesin motor.

To first confirm the functionality of the K560 construct, we conducted an MT-gliding assay, which yielded a velocity of 670 ± 10 nm/s (±SEM) at 1 mM ATP in Pipes-Hepes buffer (PHB). This is almost twice the velocity previously reported by Thorn *et al.* for the same construct in buffer containing 12 mM Pipes, 2 mM $MgCl_2$, and 1 mM EGTA (pH 6) (BRB12) (*50*), but is comparable to the value reported by Friedman *et al.* (*51*) (also in BRB12). For optical trapping experiments, the GFP moiety fused to K560 was used to specifically couple the motor to beads coated with anti-GFP antibodies. We then determined the single-molecule stall force of K560 in 80 mM Pipes, 2 mM $MgCl_2$, and 1 mM EGTA (pH 6.8) (BRB80), a buffer system typically used to study kinesin. This yielded a value of 5.7 ± 0.9 pN (±SD; stall plateaus ≥200 ms; Fig. 5, A to C), which is in agreement with the previously reported stall forces between 5 and 7 pN (*39*, *52*–*56*). In addition, both the stall forces and the detachment forces were independent of the trap stiffness in BRB80 (Fig. 5B). The stall force was also found to be ~1.4 times greater than the detachment force, which is in good agreement with the ratio reported for kinesin-1 by Furuta *et al.* (6.8/5.2 pN ~1.3, BRB12) (*55*).

When force measurements for K560 were obtained in PHB, we observed a slight dependence of the detachment force and distance on trap stiffness (Fig. 5D). However, the stall force F_s that resulted from the fit of Eq. 4 to the measured detachment forces (5.6 ± 0.1 pN, ±SEM; Fig. 5D), agreed well with the stall forces (≥200 ms) measured for the highest trap stiffness in PHB (5.7 ± 0.2 pN, mean ± SEM; 0.09 pN/nm) and with the stall force in BRB80 (Fig. 5C), indicating that the intrinsic stall force of K560 is not significantly reduced by the PHB system.

Last, to determine whether a systematic increase in buffer ionic strength results in a more pronounced effect of the trap stiffness, the PHB system was supplemented with increasing amounts of KAc. We observed a gradually heightened sensitivity to the trap stiffness with the addition of 20 to 40 mM KAc (Fig. 5D), whereas at high trap stiffnesses, the extrapolated force plateaus were similar to the stall force observed in BRB80 (Fig. 5, C and D). Only the buffer with the highest KAc concentration resulted in a significantly decreased value for F_s of 4.6 ± 0.4 pN (±SE from the fit with Eq. 4). Our data therefore suggest that kinesin's processivity becomes more and more limiting with increasing salt concentration, leading to trap stiffness–dependent forces. This hypothesis is further substantiated

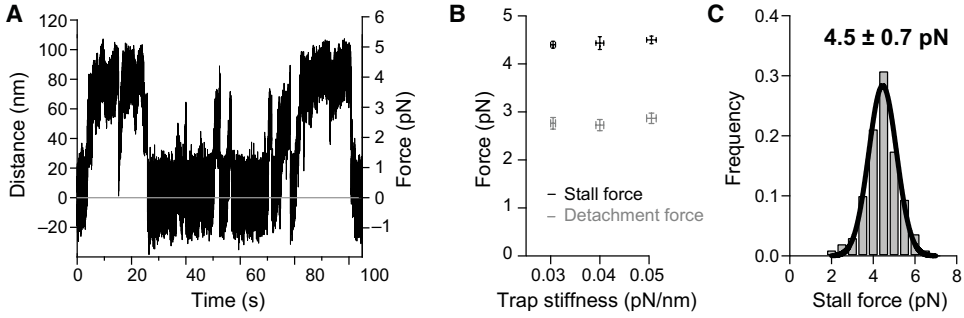

Fig. 4. Force generation of yeast dynein is insensitive to changes within a practical trap stiffness range. (**A**) Example trace showing stalling events and premature detachments of full-length yeast dynein (k = 0.05 pN/nm). Yeast dynein was specifically attached to beads coated with anti-GFP antibodies. (**B**) Forces versus trap stiffness. Values of stall forces (≥10 s, black) and of all events (gray) do not depend on the trap stiffness in the measured trap stiffness range (the error bars represent the 95% CIs of the means of the measured forces and trap stiffnesses). (**C**) Histogram of stall forces measured at various trap stiffnesses (N = 486; mean ± SD).

by the finding that the y intercepts of the hyperbolic distance fits with Eq. 5 decay with increasing [KAc], suggesting a decreased run length (Fig. 5D). These observations—in combination with the data obtained for human dynein—thus indicate that the y intercept (k = 0.00 pN/nm) in a distance versus trap stiffness plot is a measure of a motor's run length at zero load.

DISCUSSION

Human dynein is an essential motor protein that is responsible for a multitude of transport and force-generating processes within the cell (*1*, *3*). However, despite its central role in cellular biology, the biochemical and biophysical properties of dynein have not been fully deciphered. This is evidenced by the range of run lengths (*17*, *20*, *22*–*25*, *36*) and forces (*15*–*21*) (see Introduction) that have been reported for this protein.

In this study, our analysis of human dynein in the absence of cofactors suggests that the forces generated by this protein in optical trapping assays are limited by the motor's processivity. This is indicated by the hyperbolic trap stiffness dependence that is observed for the measured forces and distances. The hyperbolic force plateau for all force-generating events at an infinite trap stiffness was found to coincide with human dynein's stall force (≥200 ms force plateau) at high trap stiffnesses (1.9 ± 0.1 pN, ±SEM). High stall forces of up to 2.4 pN can be observed, even at low trap stiffness (0.01 pN/nm; see example traces in fig. S2B), but these are extremely rare. In addition, analogous to the detachment forces, our data imply that the run distance calculated for a trap stiffness of 0.00 pN/nm corresponds to dynein's run length in the absence of load (91 ± 5 nm, ±SE).

Our hypothesis that trap stiffness–dependent forces act as an indicator for limiting motor processivity is further substantiated by trapping experiments with two other molecular motors. As expected, the highly processive yeast dynein motor (*8*, *11*, *47*) did not show trap stiffness–dependent behavior in our optical trap with a reach of ~300 nm, which allowed for trap stiffnesses equal to, or above, 0.03 pN/nm. Lower trap stiffnesses resulted in the motor frequently moving out of the trap due to its high processivity and yielded forces of ~4.5 pN (see Fig. 4), thereby preventing the determination of an accurate detachment force. The processivity of the kinesin-1 motor construct, K560, in contrast, could be sufficiently modulated by the addition of potassium acetate to the buffer. As predicted, increasing amounts of salt led to a heightened dependence on trap stiffness for both the detachment forces and run distances (see Fig. 5). Although the stall forces, as determined by the force plateau of the hyperbolic plot, did not depend significantly on the salt concentration, the distances extrapolated to a trap stiffness of 0.00 pN/nm decreased with the addition of salt, suggesting a decreased run length at zero load (see Fig. 5). Thus, our observation of trap stiffness–dependent behavior for kinesin in elevated salt buffers, but not in the traditional low-salt kinesin buffer system, BRB80, reinforces the validity of our observations with human dynein. We hypothesize that such trap stiffness–dependent forces can be expected for other molecular motors with limiting processivity. However, whether such a behavior is measurable depends on a combination of parameters, including the reach of the optical trap and, thus, the range of usable trap stiffnesses, the presence of vertical force components (*57*), as well as the motor's processivity and its intrinsic stall force (see above, yeast dynein). In support of the broad relevance of this phenomenon, a similar trap stiffness–dependent behavior was reported for the molecular motor, kinesin-5 (Eg5), which generated a stall force of 1.5 pN under low-processivity conditions (*58*). Similar to human dynein in this study, Eg5 does not show clear stalling events before dissociation, indicative of low processivity (*42*).

The processivity of a motor is highly dependent on the experimental conditions under which it is measured, including the buffer system. Therefore, a range of observed forces would be expected for any given trap stiffness, depending on the buffer that is used. Moreover, different trap stiffnesses are expected to produce different observed forces in the same buffer system. Thus, the trap stiffness dependence revealed in this study could explain the range of in vitro forces, reported to be between 1 and 2 pN, for human dynein (*15*, *17*, *18*, *21*). The higher forces reported by Walter *et al.* (*16*) and Toba *et al.* (*19*), however, are not consistent with our findings at the single-molecule level. Although the reason for this is unclear, possible explanations include the presence of motor aggregates, dynein cofactors, or posttranslational modifications on purified dynein in these publications. Alternatively, contamination with other molecular motors, such as the possible copurification of kinesin-1 with our StrepTrap-purified human dynein (see Supplementary Materials and fig. S6), is difficult to completely rule out, as trace amounts of protein that are undetectable by Western blot analysis could be sufficient to account for the observed single-molecule behavior.

A recent publication (*18*) has reported that forces measured in vivo for retrograde transport by dynein cluster in 2-pN increments, and the authors attribute this to the cooperation between two dynein dimers. However, our current findings would suggest that the unit

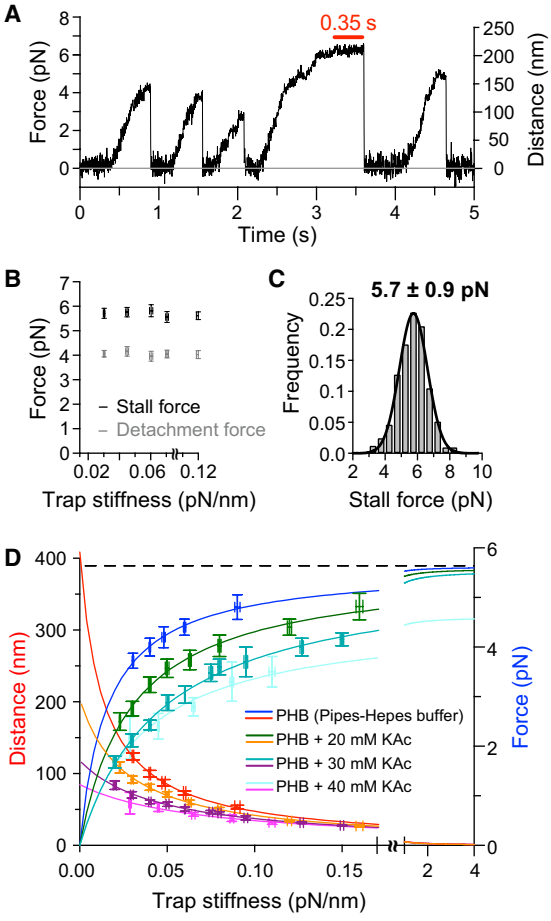

Fig. 5. Kinesin force generation becomes sensitive to changes in trap stiffness with increasing ionic strength. (**A**) Example trace of K560 in BRB80 trapping buffer showing a stalling event (red horizontal bar) and events without stalling (k = 0.03 pN/nm). (**B**) Stall forces (stalling for ≥200 ms; black crosses) and detachment forces (gray crosses) measured in BRB80 (the error bars are the 95% CIs of the mean forces and trap stiffnesses). (**C**) Stall force histogram measured in BRB80 (k = 0.03 to 0.12 pN/nm, N = 409, F_{stall} = 5.7 ± 0.9 pN; mean ± SD). (**D**) Trap stiffness dependence of all events in Pipes-Hepes trapping buffer (blue, red), Pipes-Hepes trapping buffer +20 mM KAc (green, orange), + 30 mM KAc (dark cyan, purple), and + 40 mM KAc (light blue, magenta). Fitting Eq. 4 to the detachment forces (right y axis, circles, diamonds, hexagons, and crosses) and Eq. 5 to the distances (left y axis, triangles, squares, and plus signs) reveals the same hyperbolic dependence (solid curves) on the trap stiffness as human dynein (see Fig. 3C) (the error bars are the 95% CIs of the means of the measured forces, distances, and the trap stiffnesses). The dashed line depicts the average stall force in BRB80 [5.7 ± 0.9 pN; see (C) for histogram].

force of a single dynein dimer is ~2 pN, in agreement with a recent study on recombinant full-length human dynein (*12*). Torisawa *et al.* (*26*) reported a force generation for human dynein of ~0.9 pN at a 0.01 pN/nm trap stiffness, a value that we also confirmed (Fig. 2A). However, this study further found that force generation does not change when the trap stiffness is increased to 0.028 pN/nm. Further studies will be required to resolve this apparent discrepancy.

CONCLUSION

In this study, we demonstrate that the peak force generation of mammalian cytoplasmic dynein measured in optical tweezers experiments is strongly influenced by its limited processivity and, therefore, by the trap stiffness. At relatively weak trap stiffness, true stalling is exceedingly rare, because the weakly processive motor simply detaches from the MT before reaching a sufficient displacement to achieve its maximal force. As a result, the measured peak force generation increases as the trap stiffness is increased. We develop a theoretical model to describe the force generation as a function of processivity and trap stiffness and use this model to precisely and definitively determine human dynein's stall force and its zero-load processivity. Our findings resolve a longstanding uncertainty regarding the stall force and processivity of mammalian dynein while simultaneously providing a straightforward, self-consistent methodology for analyzing the single-molecule function of this and other weakly processive molecular motors. This framework provides a much more accurate and precise estimate than the analysis of rare stalling events at low trap stiffnesses and avoids the variability associated with arbitrarily chosen definitions of stalling (*52*).

This work provides key information on the intrinsic function of human dynein that is necessary to completely understand the effects of cofactors including dynactin and BicD. Using the results and experimental framework developed here will enable future experiments to unambiguously characterize the effects of these cofactors on both processivity and force generation independently. Moreover, although we have shown here that stall force and processivity are indeed distinct functional properties, the challenges encountered with measuring the stall force of a weakly processive motor illustrate the biological importance of processivity to generating force. For example, enhanced processivity (via cofactor association or multimotor ensembles) may be required to generate substantial forces when dynein associates with cargoes via highly compliant linkages such as cell membranes, regardless of the intrinsic maximal force generation capability. In other words, the strength of the motor can only be realized to the extent it can remain attached to its MT track. Last, the characterization of intrinsic dynein function will aid our understanding of biological scenarios in which dynein associates with organelles in the absence of dynactin (*27*, *28*).

MATERIALS AND METHODS

Materials

Chemicals were obtained from Thermo Fisher Scientific or Sigma-Aldrich unless otherwise stated. All buffers were prepared using UltraPure distilled water from Life Technologies.

Human dynein-mfGFP-IC74 purification and characterization

HEK293 cells capable of doxycycline-induced mfGFP-IC74 (multifunctional GFP-tagged human cytoplasmic dynein intermediate chain) expression were obtained from T. Murayama [Department of Pharmacology, Juntendo University School of Medicine, Tokyo, Japan (*37*, *38*)]. Cytoplasmic human dynein was purified from HEK cells essentially as described in (*37*, *38*), utilizing the streptavidin tag contained in the mfGFP-IC in a one-step StrepTrap column purification (see Supplementary Materials). The purity and composition of the human dynein complex were analyzed using standard SDS-PAGE, native light blue PAGE, and Western blot analyses (see Supporting Material).

Kinesin-1 and yeast dynein purifications

Kinesin-1 [K560-GFP (*48*–*50*)] and full-length yeast dynein (VY97) were purified as described previously (*8*, *59*). Active

motors were obtained in MT-binding release assays (protocol see below).

MT-binding release assay

To further purify the motor proteins used in this study (yeast dynein VY97, kinesin-1 K560, and mfGFP-IC74 human cytoplasmic dynein), the motors were subjected to an MTBR, in which the motors were bound to MTs in a strong-binding state [mimicked by the ATP analog AMPPNP (adenylyl-imidodiphosphate)], and functional motor proteins were subsequently released in the presence of salt and ATP (see Supporting Material).

Optical trapping assay

Coverslips for optical trapping assays were cleaned and coated as previously described (*59*, *60*) using a series of cleaning steps (sonication in mucasol and plasma cleaning) followed by coating with APTES or AE-APTES [(3-aminopropyl)triethoxysilane and *N*-(2-aminoethyl)-(3-aminopropyl)triethoxysilane, respectively]. Fluorescently labeled MTs were covalently attached to the coverslips via glutaraldehyde.

Proteins were attached either nonspecifically to polystyrene beads (0.9 μm; Bangs Laboratories Inc.) or specifically via anti-GFP antibodies (fig. S4). Antibody-bound beads were prepared as described previously (*59*). Motors were diluted in pure buffer for nonspecific binding and in buffer plus β-casein (1 mg/ml) when using antibody-coated beads. β-Casein used in these buffers was purified as described previously (*59*). Motor proteins at a given dilution were incubated with the beads for 10 min on ice before adding the final trapping solution. All final trapping solutions contained an ATP regeneration system [2 mM phosphoenol pyruvate, pyruvate kinase (0.1 mg/ml)], an oxygen scavenger system [22.5 mM glucose, pyranose oxidase (3 U/ml), 90 U/ml catalase (90 U/ml)], and 10 μM Taxol. Depending on the assay, trapping buffers used were as follows: PHB [50 mM Pipes, 50 mM Hepes, 2 mM $MgCl_2$, 1 mM EGTA (pH 7.0), 10 mM dithiothreitol (DTT), 1 mM guanosine 5′-triphosphate (GTP) or varying amounts of ATP, β-casein (1 mg/ml)]; Pipes-Hepes-KAc trapping buffer [50 mM Pipes, 50 mM Hepes, 20 or 30 or 40 mM KAc, 2 mM $MgCl_2$, 1 mM EGTA (pH 7.0), 10 mM DTT, 1 mM ATP, β-casein (1 mg/ml)]; Hepes-KAc trapping buffer [30 mM Hepes, 100 mM KAc, 2 mM Mg acetate, 1 mM EGTA (pH 7.2), 10 mM DTT, 1 mM ATP, β-casein (1 mg/ml)]; and BRB80 trapping buffer [80 mM Pipes, 2 mM $MgCl_2$, 1 mM EGTA (pH 6.8), 10 mM DTT, 1 mM GTP or 1 mM ATP, β-casein (1 mg/ml)]. Trapping assays were performed at 25°C.

The optical trapping microscope was calibrated as previously discussed (*59*). Position and trap stiffness calibrations were performed for each bead tested. The trap stiffness was calculated using a "hybrid" method of calibration (*61*), combining the power spectrum and viscous drag analyses, which permits trap stiffness calibration without the need to know the drag coefficient. The microscope body is a Nikon Eclipse Ti-U. A single, custom-designed polychroic mirror guides various lasers into the objective and has high transmission bands for emission of several fluorescent dyes including Cy3/TMR (tetramethylrhodamine) to monitor TRITC (tetramethyl rhodamine isothiocyanate)–labeled MTs using a 532-nm laser. To visualize trapped beads, a 470-nm light-emitting diode lamp was used for bright-field illumination using a charge-coupled device camera. Trapping was performed with a 10-W, 1064-nm laser (IPG Photonics) chosen for its output power stability. Detection of bead position with nanometer precision is accomplished by back focal plane detection using an 830-nm laser. Data were acquired using a custom-written software in LabVIEW (National Instruments) and MATLAB (Mathworks) and analyzed using customized MATLAB software.

For the dilution curves (processivity analysis), each bead was tested for at least 4 min before judging it as "moving" or "nonmoving" bead. Error bars were calculated assuming a binomial distribution: error bar = ± sqrt $((1-f) \times f/N)$, with f being the fraction of moving beads and N the number of beads tested. Two models were fit to the data. The first equation is based on the assumption that one or more motors are required for the observed force generation (processive model, see Supporting Material for the derivation)

$$F = 1 - \exp(-\lambda c) \tag{6}$$

where F is the moving bead fraction, c is the relative motor concentration, and λ is a fitting parameter that describes the dependence on the fraction of active motors. The second equation ("nonprocessive" model) approximates those dilution curves better that result from force generation events driven by two or more motors (see Supporting Material for the derivation)

$$F = 1 - \exp(-\lambda c) - \lambda c \exp(-\lambda c) \tag{7}$$

The coefficients of determination (R^2) at a significance level $\alpha = 0.05$ and AIC test were used to judge which model approximates the data better. All figures were prepared using Prism software (GraphPad), and all fitting procedures, including the AIC test, were performed therein.

SUPPLEMENTARY MATERIALS

Supplementary material for this article is available at http://advances.sciencemag.org/cgi/content/full/6/15/eaaz4295/DC1

View/request a protocol for this paper from *Bio-protocol*.

REFERENCES AND NOTES

1. J. R. Kardon, R. D. Vale, Regulators of the cytoplasmic dynein motor. *Nat. Rev. Mol. Cell Biol.* **10**, 854–865 (2009).
2. S. R. White, B. Lauring, AAA+ ATPases: Achieving diversity of function with conserved machinery. *Traffic* **8**, 1657–1667 (2007).
3. M. A. Olenick, E. L. F. Holzbaur, Dynein activators and adaptors at a glance. *J. Cell Sci.* **132**, jcs227132 (2019).
4. J. K. Moore, J. A. Cooper, Coordinating mitosis with cell polarity: Molecular motors at the cell cortex. *Semin. Cell Dev. Biol.* **21**, 283–289 (2010).
5. J. R. Bader, K. T. Vaughan, Dynein at the kinetochore: Timing, interactions and functions. *Semin. Cell Dev. Biol.* **21**, 269–275 (2010).
6. R. B. Vallee, G. E. Seale, J.-W. Tsai, Emerging roles for myosin II and cytoplasmic dynein in migrating neurons and growth cones. *Trends Cell Biol.* **19**, 347–355 (2009).
7. K. Zhang, H. E. Foster, A. Rondelet, S. E. Lacey, N. Bahi-Buisson, A. W. Bird, A. P. Carter, Cryo-EM reveals how human cytoplasmic dynein is auto-inhibited and activated. *Cell* **169**, 1303–1314.e18 (2017).
8. S. L. Reck-Peterson, A. Yildiz, A. P. Carter, A. Gennerich, N. Zhang, R. D. Vale, Single-molecule analysis of dynein processivity and stepping behavior. *Cell* **126**, 335–348 (2006).
9. M. Nishiura, T. Kon, K. Shiroguchi, R. Ohkura, T. Shima, Y. Y. Toyoshima, K. Sutoh, A single-headed recombinant fragment of *Dictyostelium* cytoplasmic dynein can drive the robust sliding of microtubules. *J. Biol. Chem.* **279**, 22799–22802 (2004).
10. M. P. Nicholas, P. Höök, S. Brenner, C. L. Wynne, R. B. Vallee, A. Gennerich, Control of cytoplasmic dynein force production and processivity by its C-terminal domain. *Nat. Commun.* **6**, 6206 (2015).
11. C. Cho, S. L. Reck-Peterson, R. D. Vale, Regulatory ATPase sites of cytoplasmic dynein affect processivity and force generation. *J. Biol. Chem.* **283**, 25839–25845 (2008).

12. V. Belyy, M. A. Schlager, H. Foster, A. E. Reimer, A. P. Carter, A. Yildiz, The mammalian dynein–dynactin complex is a strong opponent to kinesin in a tug-of-war competition. *Nat. Cell Biol.* **18**, 1018–1024 (2016).
13. L. Rao, M. Hülsemann, A. Gennerich, Combining structure–function and single-molecule studies on cytoplasmic dynein. *Methods Mol. Biol.* **1665**, 53–89 (2018).
14. A. Gennerich, A. P. Carter, S. L. Reck-Peterson, R. D. Vale, Force-induced bidirectional stepping of cytoplasmic dynein. *Cell* **131**, 952–965 (2007).
15. B. H. Blehm, P. R. Selvin, Single-molecule fluorescence and in vivo optical traps: How multiple dyneins and kinesins interact. *Chem. Rev.* **114**, 3335–3352 (2014).
16. W. J. Walter, B. Brenner, W. Steffen, Cytoplasmic dynein is not a conventional processive motor. *J. Struct. Biol.* **170**, 266–269 (2010).
17. K. M. Ori-McKenney, J. Xu, S. P. Gross, R. B. Vallee, A cytoplasmic dynein tail mutation impairs motor processivity. *Nat. Cell Biol.* **12**, 1228–1234 (2010).
18. A. K. Rai, A. Rai, A. J. Ramaiya, R. Jha, R. Mallik, Molecular adaptations allow dynein to generate large collective forces inside cells. *Cell* **152**, 172–182 (2013).
19. S. Toba, T. M. Watanabe, L. Yamaguchi-Okimoto, Y. Y. Toyoshima, H. Higuchi, Overlapping hand-over-hand mechanism of single molecular motility of cytoplasmic dynein. *Proc. Natl. Acad. Sci. U.S.A.* **103**, 5741–5745 (2006).
20. R. Mallik, D. Petrov, S. A. Lex, S. J. King, S. P. Gross, Building complexity: An in vitro study of cytoplasmic dynein with in vivo implications. *Curr. Biol.* **15**, 2075–2085 (2005).
21. R. Mallik, B. C. Carter, S. A. Lex, S. J. King, S. P. Gross, Cytoplasmic dynein functions as a gear in response to load. *Nature* **427**, 649–652 (2004).
22. M. Trokter, N. Mücke, T. Surrey, Reconstitution of the human cytoplasmic dynein complex. *Proc. Natl. Acad. Sci. U.S.A.* **109**, 20895–20900 (2012).
23. M. Miura, A. Matsubara, T. Kobayashi, M. Edamatsu, Y. Y. Toyoshima, Nucleotide-dependent behavior of single molecules of cytoplasmic dynein on microtubules in vitro. *FEBS Lett.* **584**, 2351–2355 (2010).
24. S. J. King, T. A. Schroer, Dynactin increases the processivity of the cytoplasmic dynein motor. *Nat. Cell Biol.* **2**, 20–24 (2000).
25. J. L. Ross, K. Wallace, H. Shuman, Y. E. Goldman, E. L. Holzbaur, Processive bidirectional motion of dynein–Dynactin complexes in vitro. *Nat. Cell Biol.* **8**, 562–570 (2006).
26. T. Torisawa, M. Ichikawa, A. Furuta, K. Saito, K. Oiwa, H. Kojima, Y. Y. Toyoshima, K. Furuta, Autoinhibition and cooperative activation mechanisms of cytoplasmic dynein. *Nat. Cell Biol.* **16**, 1118–1124 (2014).
27. D. J.-K. Hu, A. D. Baffet, T. Nayak, A. Akhmanova, V. Doye, R. B. Vallee, Dynein recruitment to nuclear pores activates apical nuclear migration and mitotic entry in brain progenitor cells. *Cell* **154**, 1300–1313 (2013).
28. S. C. Tan, J. Scherer, R. B. Vallee, Recruitment of dynein to late endosomes and lysosomes through light intermediate chains. *Mol. Biol. Cell* **15**, 467–477 (2010).
29. M. van Spronsen, M. Mikhaylova, J. Lipka, M. A. Schlager, D. J. van den Heuvel, M. Kuijpers, P. S. Wulf, N. Keijzer, J. Demmers, L. C. Kapitein, D. Jaarsma, H. C. Gerritsen, A. Akhmanova, C. C. Hoogenraad, TRAK/Milton motor-adaptor proteins steer mitochondrial trafficking to axons and dendrites. *Neuron* **77**, 485–502 (2013).
30. M. A. Schlager, H. T. Hoang, L. Urnavicius, S. L. Bullock, A. P. Carter, In vitro reconstitution of a highly processive recombinant human dynein complex. *EMBO J.* **33**, 1855–1868 (2014).
31. R. J. McKenney, W. Huynh, M. E. Tanenbaum, G. Bhabha, R. D. Vale, Activation of cytoplasmic dynein motility by dynactin-cargo adapter complexes. *Science* **345**, 337–341 (2014).
32. L. A. Amos, Brain dynein crossbridges microtubules into bundles. *J. Cell Sci.* **93**, 19–28 (1989).
33. M. A. Olenick, M. Tokito, M. Boczkowska, R. Dominguez, E. L. Holzbaur, Hook adaptors induce unidirectional processive motility by enhancing the dynein-dynactin interaction. *J. Biol. Chem.* **291**, 18239–18251 (2016).
34. M. M. Elshenawy, J. T. Canty, L. Oster, L. S. Ferro, Z. Zhou, S. C. Blanchard, A. Yildiz, Cargo adaptors regulate stepping and force generation of mammalian dynein-dynactin. *Nat. Chem. Biol.* **15**, 1093–1101 (2019).
35. M. Ichikawa, Y. Watanabe, T. Murayama, Y. Y. Toyoshima, Recombinant human cytoplasmic dynein heavy chain 1 and 2: Observation of dynein-2 motor activity in vitro. *FEBS Lett.* **585**, 2419–2423 (2011).
36. T. L. Culver-Hanlon, S. A. Lex, A. D. Stephens, N. J. Quintyne, S. J. King, A microtubule-binding domain in dynactin increases dynein processivity by skating along microtubules. *Nat. Cell Biol.* **8**, 264–270 (2006).
37. T. Kobayashi, N. Morone, T. Kashiyama, H. Oyamada, N. Kurebayashi, T. Murayama, Engineering a novel multifunctional green fluorescent protein tag for a wide variety of protein research. *PLOS ONE* **3**, e3822 (2008).
38. T. Kobayashi, T. Murayama, Cell cycle-dependent microtubule-based dynamic transport of cytoplasmic dynein in mammalian cells. *PLOS ONE* **4**, e7827 (2009).
39. K. Svoboda, S. M. Block, Force and velocity measured for single kinesin molecules. *Cell* **77**, 773–784 (1994).
40. K. Svoboda, C. F. Schmidt, B. J. Schnapp, S. M. Block, Direct observation of kinesin stepping by optical trapping interferometry. *Nature* **365**, 721–727 (1993).
41. S. M. Block, L. S. Goldstein, B. J. Schnapp, Bead movement by single kinesin molecules studied with optical tweezers. *Nature* **348**, 348–352 (1990).
42. W. R. Hesse, M. Steiner, M. L. Wohlever, R. D. Kamm, W. Hwang, M. J. Lang, Modular aspects of kinesin force generation machinery. *Biophys. J.* **104**, 1969–1978 (2013).
43. F. Berger, S. Klumpp, R. Lipowsky, Force-dependent unbinding rate of molecular motors from stationary optical trap data. *Nano Lett.* **19**, 2598–2602 (2019).
44. G. Bhabha, G. T. Johnson, C. M. Schroeder, R. D. Vale, How dynein moves along microtubules. *Trends Biochem. Sci.* **41**, 94–105 (2016).
45. L. Rao, F. Berger, M. P. Nicholas, A. Gennerich, Molecular mechanism of cytoplasmic dynein tension sensing. *Nat. Commun.* **10**, 3332 (2019).
46. T. Bameta, R. Padinhateeri, M. M. Inamdar, Force generation and step-size fluctuations in a dynein motor. *J. Stat. Mech. Theory Exp.* **2013**, P02030 (2013).
47. J. R. Kardon, S. L. Reck-Peterson, R. D. Vale, Regulation of the processivity and intracellular localization of *Saccharomyces cerevisiae* dynein by dynactin. *Proc. Natl. Acad. Sci. U.S.A.* **106**, 5669–5674 (2009).
48. G. Woehlke, A. K. Ruby, C. L. Hart, B. Ly, N. Hom-Booher, R. D. Vale, Microtubule interaction site of the kinesin motor. *Cell* **90**, 207–216 (1997).
49. L. Romberg, D. W. Pierce, R. D. Vale, Role of the kinesin neck region in processive microtubule-based motility. *J. Cell Biol.* **140**, 1407–1416 (1998).
50. K. S. Thorn, J. A. Ubersax, R. D. Vale, Engineering the processive run length of the kinesin motor. *J. Cell Biol.* **151**, 1093–1100 (2000).
51. D. S. Friedman, R. D. Vale, Single-molecule analysis of kinesin motility reveals regulation by the cargo-binding tail domain. *Nat. Cell Biol.* **1**, 293–297 (1999).
52. H. W. Schroeder III, A. G. Hendricks, K. Ikeda, H. Shuman, V. Rodionov, M. Ikebe, Y. E. Goldman, E. L. Holzbaur, Force-dependent detachment of kinesin-2 biases track switching at cytoskeletal filament intersections. *Biophys. J.* **103**, 48–58 (2012).
53. H. Yardimci, M. van Duffelen, Y. Mao, S. S. Rosenfeld, P. R. Selvin, The mitotic kinesin CENP-E is a processive transport motor. *Proc. Natl. Acad. Sci. U.S.A.* **105**, 6016–6021 (2008).
54. C. M. Coppin, D. W. Pierce, L. Hsu, R. D. Vale, The load dependence of kinesin's mechanical cycle. *Proc. Natl. Acad. Sci. U.S.A.* **94**, 8539–8544 (1997).
55. K. Furuta, A. Furuta, Y. Y. Toyoshima, M. Amino, K. Oiwa, H. Kojima, Measuring collective transport by defined numbers of processive and nonprocessive kinesin motors. *Proc. Natl. Acad. Sci. U.S.A.* **110**, 501–506 (2013).
56. K. Visscher, M. J. Schnitzer, S. M. Block, Single kinesin molecules studied with a molecular force clamp. *Nature* **400**, 184–189 (1999).
57. S. Pyrpassopoulos, H. Shuman, E. M. Ostap, Modulation of kinesin's load-bearing capacity by force geometry and the microtubule track. *Biophys. J.* **118**, 243–253 (2020).
58. M. J. Korneev, S. Lakämper, C. F. Schmidt, Load-dependent release limits the processive stepping of the tetrameric Eg5 motor. *Eur. Biophys. J.* **36**, 675–681 (2007).
59. M. P. Nicholas, L. Rao, A. Gennerich, An improved optical tweezers assay for measuring the force generation of single Kinesin molecules. *Methods Mol. Biol.* **1136**, 171–246 (2014).
60. M. P. Nicholas, L. Rao, A. Gennerich, Covalent immobilization of microtubules on glass surfaces for molecular motor force measurements and other single-molecule assays. *Methods Mol. Biol.* **1136**, 137–169 (2014).
61. E. Schäffer, S. F. Nørrelykke, J. Howard, Surface forces and drag coefficients of microspheres near a plane surface measured with optical tweezers. *Langmuir* **23**, 3654–3665 (2007).
62. P. Romac, T. Žanić-Grubisić, O. Ćulić, P. Cvitković, M. Flogel, Sperm motility and kinetics of dynein ATPase in astheno- and normozoospermic samples after stimulation with adenosine and its analogues. *Hum. Reprod.* **9**, 1474–1478 (1994).
63. R. B. Case, D. W. Pierce, N. Hom-Booher, C. L. Hart, R. D. Vale, The directional preference of kinesin motors is specified by an element outside of the motor catalytic domain. *Cell* **90**, 959–966 (1997).
64. J. Howard, A. A. Hyman, Preparation of marked microtubules for the assay of the polarity of microtubule-based motors by fluorescence microscopy. *Methods Cell Biol.* **39**, 105–113 (1993).
65. R. D. Vale, Y. Y. Toyoshima, Rotation and translocation of microtubules in vitro induced by dyneins from *Tetrahymena* cilia. *Cell* **52**, 459–469 (1988).
66. A. Edelstein, N. Amodaj, K. Hoover, R. Vale, N. Stuurman, Computer control of microscopes using μManager. *Curr. Protoc. Mol. Biol.* **92**, Unit14.20 (2010).
67. E. Meijering, O. Dzyubachyk, I. Smal, Methods for cell and particle tracking. *Methods Enzymol.* **504**, 183–200 (2012).
68. M. Swoboda, J. Henig, H.-M. Cheng, D. Brugger, D. Haltrich, N. Plumeré, M. Schlierf, Enzymatic oxygen scavenging for photostability without pH drop in single-molecule experiments. *ACS Nano* **6**, 6364–6369 (2012).
69. P. Satpute-Krishnan, J. A. DeGiorgis, M. P. Conley, M. Jang, E. L. Bearer, A peptide zipcode sufficient for anterograde transport within amyloid precursor protein. *Proc. Natl. Acad. Sci. U.S.A.* **103**, 16532–16537 (2006).
70. T. Shimizu, Y. Y. Toyoshima, M. Edamatsu, R. D. Vale, Comparison of the motile and enzymatic properties of two microtubule minus-end-directed motors, ncd and cytoplasmic dynein. *Biochemistry* **34**, 1575–1582 (1995).

71. H. S. Shpetner, B. M. Paschal, R. B. Vallee, Characterization of the microtubule-activated ATPase of brain cytoplasmic dynein (MAP 1C). *J. Cell Biol.* **107**, 1001–1009 (1988).
72. J. Roostalu, C. Hentrich, P. Bieling, I. A. Telley, E. Schiebel, T. Surrey, Directional switching of the kinesin Cin8 through motor coupling. *Science* **332**, 94–99 (2011).
73. H. Kojima, E. Muto, H. Higuchi, T. Yanagida, Mechanics of single kinesin molecules measured by optical trapping nanometry. *Biophys. J.* **73**, 2012–2022 (1997).
74. L. A. Ligon, M. Tokito, J. M. Finklestein, F. E. Grossman, E. L. F. Holzbaur, A direct interaction between cytoplasmic dynein and kinesin I may coordinate motor activity. *J. Biol. Chem.* **279**, 19201–19208 (2004).
75. A. J. Firestone, J. S. Weinger, M. Maldonado, K. Barlan, L. D. Langston, M. O'Donnell, V. I. Gelfand, T. M. Kapoor, J. K. Chen, Small-molecule inhibitors of the AAA+ ATPase motor cytoplasmic dynein. *Nature* **484**, 125–129 (2012).
76. B. M. Paschal, H. S. Shpetner, R. B. Vallee, MAP 1C is a microtubule-activated ATPase which translocates microtubules in vitro and has dynein-like properties. *J. Cell Biol.* **105**, 1273–1282 (1987).
77. S. C. Kuo, M. P. Sheetz, Force of single kinesin molecules measured with optical tweezers. *Science* **260**, 232–234 (1993).
78. V. Belyy, N. L. Hendel, A. Chien, A. Yildiz, Cytoplasmic dynein transports cargos via load-sharing between the heads. *Nat. Commun.* **5**, 5544 (2014).
79. W. P. Wong, K. Halvorsen, The effect of integration time on fluctuation measurements: Calibrating an optical trap in the presence of motion blur. *Opt. Express* **14**, 12517–12531 (2006).
80. M. P. Nicholas, F. Berger, L. Rao, S. Brenner, C. Cho, A. Gennerich, Cytoplasmic dynein regulates its attachment to microtubules via nucleotide state-switched mechanosensing at multiple AAA domains. *Proc. Natl. Acad. Sci. U.S.A.* **112**, 6371–6376 (2015).
81. O. K. Dudko, G. Hummer, A. Szabo, Intrinsic rates and activation free energies from single-molecule pulling experiments. *Phys. Rev. Lett.* **96**, 108101 (2006).
82. O. K. Dudko, G. Hummer, A. Szabo, Theory, analysis, and interpretation of single-molecule force spectroscopy experiments. *Proc. Natl. Acad. Sci. U.S.A.* **105**, 15755–15760 (2008).
83. G. I. Bell, Models for the specific adhesion of cells to cells. *Science* **200**, 618–627 (1978).
84. S. Klumpp, C. Keller, F. Berger, R. Lipowsky, Molecular motors: Cooperative phenomena of multiple molecular motors, in *Multiscale Modeling in Biomechanics and Mechanobiology* (Springer, London, 2014), vol. 8.
85. A. Kunwar, S. K. Tripathy, J. Xu, M. K. Mattson, P. Anand, R. Sigua, M. Vershinin, R. J. McKenney, C. C. Yu, A. Mogilner, S. P. Gross, Mechanical stochastic tug-of-war models cannot explain bidirectional lipid-droplet transport. *Proc. Natl. Acad. Sci. U.S.A.* **108**, 18960–18965 (2011).
86. S. A. Burgess, M. L. Walker, H. Sakakibara, P. J. Knight, K. Oiwa, Dynein structure and power stroke. *Nature* **421**, 715–718 (2003).
87. J. Fan, L. A. Amos, Antibodies to cytoplasmic dynein heavy chain map the surface and inhibit motility. *J. Mol. Biol.* **307**, 1317–1327 (2001).

Acknowledgments: We thank T. Murayama for generously providing the HEK293 cell line capable of doxycycline-induced mfGFP-IC74 expression. **Funding:** We were supported by the National Institutes of Health (NIH) grant R01GM098469. M.P.N. received support from the NIH-funded Medical Scientist Training and Molecular Biophysics Training programs at the Albert Einstein College of Medicine (NIH grants T32GM007288 and T32GM008572, respectively). L.R. and S.B. received support from the NIH grant R01GM098469. S.B. received support from the German Research Foundation grant BR 4257/1-1. **Author contributions:** S.B., F.B., M.P.N., and A.G. designed the research. S.B., F.B., L.R., and A.G. performed the research, S.B. and L.R. produced and purified protein. S.B., F.B., M.P.N., and A.G analyzed the data and wrote the manuscript. **Competing interests:** All authors declare that they have no competing interests. **Data and materials availability:** All data needed to evaluate the conclusions in the paper are present in the paper and/or the Supplementary Materials. Additional data related to this paper may be requested from the authors.

Submitted 8 September 2019
Accepted 22 January 2020
Published 8 April 2020
10.1126/sciadv.aaz4295

Citation: S. Brenner, F. Berger, L. Rao, M. P. Nicholas, A. Gennerich, Force production of human cytoplasmic dynein is limited by its processivity. *Sci. Adv.* **6**, eaaz4295 (2020).

Supporting Material

Human dynein mfGFP-IC74 purification and characterization

HEK 293 (human embryonic kidney 293) cells capable of doxycycline-induced mfGFP-IC74 (mf: multifunctional) expression were obtained from Prof. Takashi Murayama (Department of Pharmacology, Juntendo University School of Medicine, Tokyo, Japan (*37*, *38*)). Human cytoplasmic dynein was purified from HEK cells essentially as described (*37*, *38*). In short, mfGFP-IC74 expression was induced in HEK cells grown to 70-80% confluency using 2 µg/ml doxycycline for 48 hours. Cells were harvested by trypsinization, washed with phosphate-buffered saline, and frozen in liquid nitrogen. The multifunctional mfGFP-IC74 chain includes the streptavidin-binding peptide thus allowing for a one-step purification of the dynein-IC74 complex on a streptavidin column. The cell pellet of eight 150 mm HEK dishes was used for a single purification on a 1 ml StrepTrap HP column (GE Healthcare Biosciences). Cells were defrosted and resuspended in buffer A (25 mM Tris-HCl, 150 mM NaCl, 0.3 M sucrose, 5 mM MgSO4, 1 mM DTT, pH 7.5) in the presence of 1 Complete Mini Protease Inhibitor tablet (Roche) per 10 ml of cell lysate, 0.05% Triton-X100, and 0.5 mM ATP. Manual homogenization was performed on ice using a glass-teflon homogenizer (15-20 strokes). Cell debris was removed in an ultracentrifuge spin (30 min, 4^{o}C, 100,000 x g, Optima TLX centrifuge (Beckman Coulter)), the resulting supernatant was filtered using a syringe filter with a 0.45 µm pore size (Millipore) and applied onto the 1 ml StrepTrap column pre-equilibrated with buffer A. The column was washed with 5 column volumes (*62*) buffer A (wash fraction 1 (W1)), followed by 5 CV buffer A + 500 mM NaCl (W2), and 5 CV buffer A (W3). The dynein complex was eluted with 2.5 mM desthiobiotin in buffer A. Elution fractions were collected manually (~0.5 ml/fraction) and tested for protein using a mini-Bradford assay in a micro-plate (Coomassie reagent and plate from ThermoScientific). Protein-containing fractions were frozen in small aliquots in liquid nitrogen and stored at -80^{o}C.

Gel and Western Blot analysis

The purity of the human dynein complex was analyzed on a 4-12% Bis-Tris SDS gel (Life Technologies) using InstaBlue protein stain (Expedeon) (Fig. S1A). The oligomerization state was determined on a Native Light Blue PAGE (Life Technologies) using the manufacturer's standard procedure, Native Mark (Life Technologies) as protein standard, and a regular silver-stain protocol to visualize small amounts of protein (Fig. S1B).

The presence of subunits and cofactors was analyzed using standard Western Blot analysis (Fig. S1C). 10 µl of StrepTrap-released dynein was run on a 4-12% Bis-Tris gel in each lane. Proteins were transferred onto a double-layer of Protran BA 85 nitrocellulose membranes (0.45 µm pore size, Whatman) over night at 4^{o}C using 30 V for probing proteins >50 kDa and for 45 min at RT using 200 V for proteins <50 kDa in a BioRad Western Blot transfer system. Precision Plus Protein Dual Color Standard (BioRad) was co-transferred to estimate the molecular weight of the bands. The primary antibodies used were as follows: HC, anti-dynein heavy chain (5 µg/ml final concentration; raised against the N-terminal tail in

rabbit); IC, anti-intermediate chain (1 µg/ml, MAB1618, Millipore); GFP, anti-GFP (1 µg/ml, MAB1083, Millipore); LC, anti-light chain (0.2 µg/ml, ab51603, Abcam); LIC, anti-light intermediate chain (1 µg/ml, ab123901, Abcam); p150, anti-p150glued (2 µg/ml, PA518095, ThermoScientific); Lis1, anti-Lis1 (1 µg/ml, clone Lis1-388, Sigma); Nde1, anti-Nde1 (0.45 µg/ml, 10233-1-AP, ProteinTech). Secondary Alexa-488-labeled antibodies (0.4 µg/ml; Life Technologies) were used for fluorescent detection in a LI-COR Odyssey scanner (LI-COR Biosciences).

MT-gliding assay

As a first test of human dynein's motile properties, we performed MT-gliding assays with StrepTrap-released dynein in a total internal reflection fluorescence (TIRF) microscope (Fig. S7C). Microtubules (MTs) were polymerized from purified bovine or porcine tubulin (Cytoskeleton) using 20 µg TRITC (tetramethyl rhodamine isothiocyanate)-labeled tubulin and 20 µl 10 mg/ml unlabeled tubulin in BRB80 (80 mM Pipes**,** 2 mM $MgCl_2$**,** 1 mM EGTA**,** pH 6.8). Polymerization was induced by addition of 1 mM Mg-GTP (Cytoskeleton) for 20 min at 37°C. MTs were stabilized by adding 20 µM paclitaxel (taxol, tx, Cytoskeleton) for 20 min at 37°C and separated from unpolymerized tubulin by spinning the solution over a 60% glycerol cushion including 20 µM tx (60% (V/V) glycerol in BRB80; 80 krpm in rotor TLA100, Optima TLX centrifuge (Beckman Coulter), 10 min, 25°C). The resulting MT pellet was resuspended in BRB80 + 20 µM tx and stored at room temperature for up to two weeks. Polarity-marked MTs were prepared as described in (*63-65*) and on the Mitchison laboratory website (https://mitchison.hms.harvard.edu/microtubules).

The total internal reflection fluorescence (TIRF) microscope used for the MT-gliding assays was a Nikon Eclipse Ti E/B equipped with a 512 x 512 pixel EMCCD camera (Andor iXON ULTRA, 16 µm pixel size). The field of view was 81.92 x 81.92 μm^2 (100x magnification) and a 532 nm laser (Coherent Sapphire) was used to illuminate TRITC-labeled MTs. Videos were acquired using the Micromanager software package (ImageJ, National Institute of Health (*66*)) with an acquisition rate of 1 frame/s and analyzed in ImageJ using the plug-in MTrackJ (*67*).

For the MT-gliding assay, coverslips (Zeiss) were cleaned using an HCl-EtOH cleaning procedure as described on the Salmon Lab website (http://labs.bio.unc.edu/Salmon/protocolscoverslippreps.html). Briefly, coverslips were washed in 1 M HCl at 60°C overnight, washed and sonicated in ddH_2O (3 x 30 min) and further cleaned by sonication in solutions with increasing EtOH content (30 min each in 50% EtOH, 70% EtOH, and 100% EtOH). 200 proof EtOH (Fisher) was used for all solutions. Clean coverslips were stored in 200 proof EtOH at room temperature and flamed immediately before use. Flow chambers were prepared by sandwiching two parallel stripes of double-sided sticky tape (Scotch) between a glass slide (Fisher Scientific) and a coverslip. Before starting the microscope experiments, flow chambers were sealed with vacuum grease (Dow Corning).

The StrepTrap-released dynein was bound to coverslips non-specifically onto a surface pre-treated with 0.01 mg/ml bovine serum albumin (BSA). After binding the dynein motors, the coverslip surface was blocked with 2 mg/ml BSA in Pipes-Hepes MT-gliding buffer (50 mM Pipes, 50 mM Hepes, 2 mM $MgCl_2$,

1 mM EGTA, pH 7.0, 1 mM DTT, 1 mM ATP, 2 mg/ml BSA, 2 mM phosphoenol pyruvate, 0.1 mg/ml pyruvate kinase, 23 mM glucose, 3 U/ml pyranose oxidase, 90 U/ml catalase (*68*)). MT-gliding assays were performed at room temperature using ~450 nM MTs (final concentration, ~5 mg/ml) and varying amounts of ATP (Fig. S7B). An ATP-concentration dependence of the MT-gliding velocity resulted in a Michaelis-Menten constant of K_M (*69*) = 39 ± 4 μM and a maximum velocity of v_{max} = 1.10 ± 0.03 μm/s (R^2 = 0.996; values ± SE from fit; Fig. S7A). These Michaelis-Menten parameters are in the range of previously reported values for mammalian dyneins (*19, 22, 26, 38, 70, 71*). Furthermore, movement was exclusively minus end-directed (70/70 polarity-marked MTs; Fig. S7C), thus confirming the basic activity of our human dynein preparation.

The buffer system was optimized for high velocities, while retaining continuous gliding and good MT surface attachment. Best results were obtained with the chosen Pipes-Hepes buffer (50 mM Pipes, 50 mM Hepes, 2 mM $MgCl_2$, 1 mM EGTA, pH 7.0), as MT-gliding was smooth and the gliding MTs were rarely released from the coverslip surface. In contrast, at the same dynein surface density MT-gliding became increasingly wobbly in buffers with increased salt concentration, MTs were not attached across their entire length and dissociated frequently indicative of decreased motor processivity. In other tested buffer systems, MT-gliding velocities were reduced compared to Pipes-Hepes (e.g. BRB80 yielded only <50% of v_{max} in Pipes-Hepes). Therefore, we chose to perform all subsequent experiments in Pipes-Hepes buffer prepared with Life Technologies UltraPure distilled water.

Bidirectional force generation by StrepTrap-released human dynein fraction

In initial optical trapping experiments, undiluted StrepTrap-released dynein was bound non-specifically to carboxyl-beads. In contrast to dynein's MT-gliding activity, which was exclusively minus end-directed (see above and Fig. S7), we observed force generation both toward the MT minus end and toward the plus end (Fig. S6A). Four independent dynein StrepTrap purifications were tested yielding up to 30% plus end-directed force generation (bead statistics for a particular purification see Table S1). While there have been previous reports of bidirectional force generation by molecular motors either due to high motor concentrations (*10, 72*) or due to an ion-dependent mechanistic change (*18*), our detailed analysis of the observed behavior suggests that we were dealing with a kinesin-1 contamination in the dynein StrepTrap release fraction as discussed below (see also Fig. S6 and Table S1).

The observed plus end-directed forces were significantly larger than minus end-directed events with stall forces frequently observed at ~5-6 pN and traces resembling those of purified kinesin-1 (Fig. S6C) (52, *53, 73*). To determine whether the plus end-directed motion was caused by trace amounts of kinesin-1 co-purified by a direct interaction between dynein's IC and kinesin-1's light chains (*74*), we sought to find experimental conditions, in which dynein motility is significantly inhibited. While the reported dynein inhibitor Ciliobrevin D (*75*) did not sufficiently reduce dynein's MT-gliding velocity at inhibitor concentrations up to 250 μM (MT-gliding velocities still >100 nm/s), we found that using 1 mM GTP instead of ATP as fuel (*71, 76*) decreased dynein's MT-gliding velocity ~112-fold (Fig. S6D and

Table S1). In contrast, purified kinesin-1 (K560-GFP)'s MT-gliding velocity was only reduced <6-fold in the presence of 1 mM GTP (see also (*39*, *77*)) (Fig. S6E), thus providing an experimental tool to distinguish kinesin- from dynein-related events. Subsequent optical trapping experiments with the human StrepTrap release fraction in the presence of GTP demonstrated that the number of minus end-directed force generation events were significantly reduced and that their interaction times were increased 52-fold (Fig. S6F). In contrast, displacements toward the plus end were prolonged merely by a factor of 4 (Fig. S6G), suggesting that plus end-directed motion was kinesin-related. Moreover, initial bead velocities determined at 1 mM ATP and 1 mM GTP revealed a close approximation between the plus end-directed motility in our StrepTrap release fraction and purified kinesin-1 (Fig. S6H). Stall forces for plus end-directed motion were somewhat lower (stall force F_{stall} = 4.8 ± 0.9 pN; ± SD) than for purified kinesin-1 (F_{stall} = 5.8 ± 0.9 pN; ± SD) (Fig. S6I), which may be explained by dynein motors bound to the same bead resisting kinesin's force production in agreement with previous reports (*15*).

Plus end-directed bead motion was not observed when StrepTrap-released dynein was bound to beads specifically via anti-GFP antibodies (Fig. S4). Moreover, when the StrepTrap-released dynein was subjected to a MT-binding and release (MTBR) assay (see below), the resulting dynein solution no longer displayed any plus end-directed events (hundreds of tested beads), even when bound non-specifically to carboxyl-beads. Although mass spectrometric analyses did not detect kinesin-1, our data suggest that trace amounts of contaminating kinesin-1 motors were responsible for the observed plus end-directed forces. All subsequent optical trapping studies were therefore performed with MTBR-purified human dynein to eliminate plus end-directed force generation and to prevent any influence of dynein cofactors.

MT-binding and release

To further purify the motor proteins used in this study (yeast dynein VY97, kinesin-1 K560, and mfGFP-IC74 human cytoplasmic dynein), the motors were subjected to a MTBR, in which the motors were bound to MTs in a strong-binding state (mimicked by the ATP-analog AMPPNP, Adenylyl-imidodiphosphate) and functional motor proteins were subsequently released in the presence of ATP (Fig. S1D). Purified undiluted protein solutions were supplemented with 20 µM tx, 1 mM AMPPNP, and 3 µM MTs and spun for 5 min in an ultracentrifuge (Optima TLX centrifuge (Beckman Coulter) in rotor TLA100, 40 krpm, room temperature). The resulting MT pellet was resuspended in BRB12 (12 mM Pipes, 2 mM $MgCl_2$, 1 mM EGTA, pH 6.8) plus 20 µM tx and 1 mM DTT and spun again to remove AMPPNP. The obtained MT pellet was resuspended in 30 mM Hepes, 200 mM KCl, 2 mM $MgCl_2$, 10% glycerol, 1 mM DTT, 20 µM tx, 10 mM ATP, pH 7.4. After a final ultracentrifuge spin, the resulting supernatant contained (predominantly) active motor proteins. Samples were taken at each step and analyzed on a 4-12% Bis-Tris SDS-PAGE (Life Technologies) stained with InstaBlue stain (Expedeon).

Yeast dynein stall forces

For full-length yeast dynein (yeast strain VY97 genotype: *MATa {leu2-3,112 trp1-1 can1-100 ura3-1 ade2-1 his3-11,15} [phi+] pep4Δ::HIS3, prb1Δ, PAC11-13xMyc::TRP, ZZ-TEV-GFP-3xHA-DYN1*), we measured the stall force to be 4.5 ± 0.7 pN, somewhat lower than we previously measured using a different instrument (*14*), but similar to recent reports (*13*, *78*). We attribute the difference to an erroneous calibration of the previous instrument, caused by unintended electronic low-pass filtering during data acquisition, leading to an overestimation of the trap stiffness (*59*, *79*) as described below.

To prevent aliasing during data acquisition in optical trapping experiments, low-pass filtering is commonly employed at half the data sampling rate. During calibration, however, it is critical that the filtering frequency be sufficiently high (at least 50-100 kHz for 500-1000 nm bead diameters) that significant high-frequency components of the bead's motion are not discarded. Such filtering reduces the apparent variance of the bead's Brownian motion, $\mathrm{Var}(x)$, leading to an overestimation of the trap stiffness, especially when calculated via the equipartition method, i.e. $k = k_\mathrm{B}T/\mathrm{Var}(x)$ (where k is the trap stiffness, k_B is the Boltzmann constant, T is the temperature in Kelvin, and $k_\mathrm{B}T = 4.116$ pNnm at 25 °C; see ref. 32 for a detailed discussion). In practice, this error may be partially counterbalanced by low-frequency drift that erroneously increases the measured Var(*x*). In our previous work (*14*), the same filter settings were used for both calibration and data acquisition. In that work, data were sampled at 2 kHz and low-pass filtered at 1 kHz.

An estimation of the error in stall force measurement can be performed as follows. Parseval's Theorem states that $\mathrm{Var}(x)$ is equal to the the integral ("area under the curve") of the power spectral density, $S_{xx}(f)$, of the Brownian motion, i.e. $\mathrm{Var}(x) = \int_0^\infty S_{xx}(f)df$, where f is the frequency. One may thus consider that $\mathrm{Var}(x)$ is reduced by low-pass filtering due to truncation of the power spectrum above the low-pass filter frequency F and concomitant loss of the associated area under the curve. The ratio Q of the measured variance $\mathrm{Var}_\mathrm{Measured}(x)$ to the true variance $\mathrm{Var}_\mathrm{True}(x)$ is

$$Q = \frac{\int_0^F S_{xx}(f)df}{\int_0^\infty S_{xx}(f)df} \qquad \text{Eq. 1}$$

and thus the true trap stiffness $k_\mathrm{True} = Qk_\mathrm{Measured}$. It can be shown that $S_{xx}(f)$ assumes a Lorentzian form,

$$S_{xx}(f) = \frac{k_BT}{\pi^2\gamma(f_c^2+f^2)} \qquad \text{Eq. 2}$$

where γ is the drag coefficient for the bead, and $f_c = k/2\pi\gamma$ is the characteristic "corner" frequency for the spectral density function (frequency at which the function reaches half its maximum value). Thus, $k = 2\pi\gamma f_c$. The numerator of Q is

$$\int_0^F S_{xx}(f)df = \frac{k_BT}{\pi^2\gamma f_c}\arctan(F/f_c) \qquad \text{Eq. 3}$$

and the denominator is simply

$$\mathrm{Var}(x) = \frac{k_BT}{k} = \frac{k_BT}{2\pi\gamma f_c} \qquad \text{Eq. 4}$$

and thus

$$Q = \frac{2\arctan(F/f_c)}{\pi}. \quad \text{Eq. 5}$$

Substituting $f_c = k_{\text{True}}/2\pi\gamma$ and $Q = k_{\text{True}}/k_{\text{Measured}}$ yields

$$k_{\text{True}} = \frac{2}{\pi}\arctan\left[\frac{2\pi\gamma F}{k_{\text{True}}}\right]k_{\text{Measured}}. \quad \text{Eq. 6}$$

In bulk solution, the bead drag coefficient γ_0 is a function of the bead diameter (d=1000 nm in our prior work) and solution viscosity ($\eta = 8.9 \times 10^{-10}\text{pNs/nm}^2$ at 25 °C) such that $\gamma_0 = 3\pi d\eta$. However, at distance Z_B from a plane surface (i.e. the microscope coverslip), the actual drag is given by Faxén's law:

$$\gamma = \frac{\gamma_0}{1-\frac{9}{16}R+\frac{1}{8}R^3-\frac{45}{256}R^4-\frac{1}{16}R^5}, \quad \text{Eq. 7}$$

where R is the dimensionless quantity $d/(d+2Z_B)$. Assuming a working distance above the coverslip $Z_B = 185$ nm (in our previous work, the experiments were performed ~25 nm above ~160-nm thick axonemes) and a low-pass frequency $F = 1000$ Hz, we then have

$$k_{\text{True}} = 0.64\arctan\left[\frac{0.09163\text{ pN/nm}}{k_{\text{True}}}\right]k_{\text{Measured}}. \quad \text{Eq. 8}$$

Solving this equation numerically demonstrates that for $k_{\text{Measured}} \approx 0.055$ pN/nm (as in our previous work), $k_{\text{True}} \approx 0.04$ pN/nm. Thus, a measured stall force of ~7 pN was truly ~5 pN, consistent with our present results.

In the present work, we have carefully avoided calibration errors and verified precise and accurate calibration via multiple methods, all of which we have detailed (including providing example calibration data) in previous work (*59*). For the experiments reported here and our recent studies (*10, 45, 59, 80*), *F* = 32768 Hz (during calibration only) and $Z_B = 50$ nm (25 nm above the 25-nm thick surface-bound microstubules), and the discrepancy between k_{Measured} and k_{True} due to filtering is negligible (less than 2% error even for the greatest trap stiffness used of 0.1 pN/nm).

Derivation of the probability density of the detachment forces

To derive the probability density function (pdf) of the detachment forces of a molecular motor in an optical trap, we extend a theoretical framework originally developed to describe force-spectroscopy experiments of receptor-ligand bonds (*81, 82*). We introduce a binding probability *S*(*t*), which is the probability that the motor is still bound at time *t*. This binding probability is related to the pdf *p*(*F*) of the detachment forces by

$$p(F)dF = -\dot{S}(t)dt, \quad \text{Eq. 9}$$

where $\dot{S} \equiv dS/dt$. Assuming a first-order rate equation with a force-dependent unbinding rate $\varepsilon(F)$, the binding probability evolves in time as

$$\dot{S}(t) = -\varepsilon\big(F(t)\big)S(t). \quad \text{Eq. 10}$$

Using the condition $S(0) = 1$ that the motor is bound at the beginning of a trajectory, we can combine Eqs. 9 and 10 to obtain the unbinding rate

$$\varepsilon(F) = \frac{\dot{F}p(F)}{1-\int_0^F p(F\prime)dF\prime}, \quad \text{Eq. 11}$$

in which $\dot{F}$ is the force-dependent loading rate. Next, we solve this equation for the pdf

$$p(F) = \frac{\varepsilon(F)}{\dot{F}} \exp\left(-\int_0^F \frac{\varepsilon(F\prime)}{\dot{F}\prime} dF'\right). \quad \text{Eq. 12}$$

A. Detachment forces measured in a stationary optical trap

In a stationary optical trap, a molecular motor pulls a bead out of the trap center until the motor unbinds from its filament and the bead snaps back to the center of the trap. While the motor is pulling the bead, the force on the motor is increasing which in turn influences the force-dependent dynamics of the motor. Therefore, the force-dependent loading rate on the motor-filament bond is given by

$$\dot{F} = k_{\text{eff}} v_{\text{m}}(F), \quad \text{Eq. 13}$$

in which k_{eff} is the effective stiffness of the trap and the motor molecule and $v_{\text{m}}(F)$ the force-velocity relation of the motor (*43*). Combining Eqs. 12 and 13, we obtain the pdf of the detachment forces for a molecular motor in a stationary optical trap,

$$p(F) = \frac{\varepsilon(F)}{k_{\text{eff}} v_{\text{m}}(F)} \exp\left(-\int_0^F \frac{\varepsilon(F\prime)}{k_{\text{eff}} v_{\text{m}}(F\prime)} dF'\right). \quad \text{Eq. 14}$$

We recently investigated how different bond behaviors can be inferred from the pdf (*43*). However, the pdf depends on quantities that are not readily accessible in a typical trapping experiment, such as the compliance of the motor that contributes to k_{eff} and the force-velocity relation of the motor. Therefore, we derive a pdf that is a function of the trap stiffness, the unbinding rate, and the force-velocity relation of the bead (not of the motor). Assuming the optical trap can be approximated as a linear spring with trap stiffness k, the force is given by $F = kx_{\text{b}}$, in which x_{b} is the position of the bead measured as the distance from the trap center. Because the position of the bead is a function of time, we determine the total derivative for the loading rate as

$$\dot{F} = \frac{\partial F}{\partial x_{\text{b}}} \frac{dx_{\text{b}}}{dt} = k v_{\text{b}}, \quad \text{Eq. 15}$$

in which v_{b} is the force-velocity relation of the bead. Combining this expression with Eq. 12, we obtain the pdf for the detachment forces as

$$p(F) = \frac{\varepsilon(F)}{k v_{\text{b}}(F)} \exp\left(-\int_0^F \frac{\varepsilon(F\prime)}{k v_{\text{b}}(F\prime)} dF'\right). \quad \text{Eq. 16}$$

Using this pdf, we formally derive the average detachment forces

$$\langle F \rangle = \int_0^\infty F p(F) dF = \int_0^{F_{\text{s}}} F \frac{\varepsilon(F)}{k v_{\text{b}}(F)} \exp\left(-\int_0^F \frac{\varepsilon(F\prime)}{k v_{\text{b}}(F\prime)} dF'\right) dF, \quad \text{Eq. 17}$$

in which F_s is the "stall force" of the motor at which motor movement ceases. As F_s is the maximum force that the motor generates, $p(F)$ is zero for $F > F_s$ and the limit of the integration can be set to an interval from zero to F_s.

B. Average detachment force for different bond behaviors

To obtain an explicit solution for the average detachment force $\langle F \rangle$ as a function of k, we need functional forms for the unbinding rate $\varepsilon(F)$ and the force-velocity relation $v_\mathrm{b}(F)$. As an approximation for $v_\mathrm{b}(F)$, we choose the linearly decreasing function

$$v_\mathrm{b} = v_0\left(1 - {}^{F}/_{F_s}\right), \qquad \text{Eq. 18}$$

which has been extensively used for biophysical modeling of cytoskeletal motors (*83, 84*) and which is in good agreement with our experimental data (Fig. 3D). We next assume a functional form for $\varepsilon(F)$. To obtain an analytical solution for $\langle F \rangle$, we first choose the force-independent rate

$$\varepsilon(F) = \varepsilon. \qquad \text{Eq. 19}$$

Using Eqs. 18 and 19 in Eq. 17, we obtain

$$\langle F \rangle = \int_0^{F_\mathrm{s}} F \frac{\varepsilon(F)}{k v_\mathrm{b}(F)} \exp\left(\frac{\varepsilon F_s}{k v_0}[\ln(F - F_s) - \ln(F_s)]\right) dF = \frac{F_s k v_0}{\varepsilon F_s + k v_0}. \qquad \text{Eq. 20}$$

Introducing the force-free run length $x_0 = v_0/\varepsilon$, we finally obtain for $\langle F \rangle$:

$$\langle F \rangle = \frac{F_s}{1 + \frac{F_s}{k x_0}}. \qquad \text{Eq. 21}$$

We next assume an unbinding rate that exponentially increases with force and solve $\langle F \rangle$ numerically. Here, $\varepsilon(F)$ is given by

$$\varepsilon(F) = \varepsilon_0 \exp(F/F_\mathrm{d}), \qquad \text{Eq. 22}$$

in which ε_0 is the force-free unbinding rate and F_d the characteristic force, often called "detachment force". While experimental data are not available for human dynein, an exponentially increasing unbinding rate up to F_s has been reported for rat dynein (*85*). Using Eq. 22 and the linear force-velocity relation (Eq. 18), we determine the pdf of the detachment forces

$$p(F) = \frac{\varepsilon_0 F_\mathrm{s} \exp(F/F_\mathrm{d})}{k v_0 (F_\mathrm{s} - F)} \exp\left[-\frac{\varepsilon_0 F_\mathrm{s} \exp(F_\mathrm{s}/F_\mathrm{d})}{k v_0}\left(I\left(\frac{F_\mathrm{s} - F}{F_\mathrm{d}}\right) - I\left(\frac{F_\mathrm{s}}{F_\mathrm{d}}\right)\right)\right], \qquad \text{Eq. 23}$$

with the exponential integral

$$I(x) = \int_x^\infty t^{-1} \exp(-t) dt. \qquad \text{Eq. 24}$$

Because this pdf involves exponential integral functions, we are not able to derive an analytical solution for $\langle F \rangle$ and instead solve $\langle F \rangle$ as a function of k numerically, which is computationally intensive (fitting the experimental data in Fig. 3C takes a few days). For each minimization step during the fitting procedure, two integrals have to be solved numerically. When performing the fit with the numerically calculated functions, we obtain $F_s = 2.1 \pm 0.2$ pN, $x_0 = 110 \pm 30$ nm, and $F_d = 2 \pm 2$ pN (± SEM, Fig. S5). These values are within the errors of the numbers we obtain when fitting our experimental data to Eq. 21, i.e. when assuming a constant unbinding rate ($F_s = 1.9 \pm 0.1$ pN and $x_0 = 87 \pm 6$ nm, ± SEM, see main text). The large error of the estimated characteristic force F_d implies that the data do not constrain this parameter sufficiently. However, the estimates for the stall force F_s and the force-free run length x_0 have small errors and are similar for both models. Therefore, we conclude that while we cannot obtain a precise estimate for the force-dependent unbinding rate, we can obtain reasonable accurate estimates for the stall force and the force-free run length. The fact that the stall force and the force-free run length are similar for both models suggest that these parameters are largely independent of the force-dependency of the unbinding rate. Thus, a constant unbinding rate is a reasonable approximation when determining the stall force and the force-free run length of mammalian dynein.

Optical tweezers experiments at the single-molecule level

Optical trapping experiments were performed at motor dilutions at which the fraction of beads moving was ≤ 0.3. As our calculations show below, the probability that the observed movements at these dilutions is due to single dynein molecules is >99.9996%.

To determine the probability that two or more motors contribute to force generation at this motor dilution, we use the Poisson distribution

$$P(x, \rho) = \frac{\rho^x e^{-\rho}}{x!}, \quad \text{Eq. 25}$$

with ρ being the average rate and x the number of events, to calculate the chances that any given bead has at least one motor bound (one or more) at the motor concentration *C*:

$$P_1 = P(x > 0, C) = 1 - P(x = 0, C) = 1 - \frac{C^0 e^{-C}}{0!} = 1 - e^{-C}. \quad \text{Eq. 26}$$

Thus, if one motor is enough to move a bead, the fraction *F* of moving beads as a function of the relative motor concentration $c = C/\lambda$ is

$$F_1(c) = P_1 = 1 - e^{\lambda c}, \quad \text{Eq. 27}$$

with λ is a fitting parameter that describes the dependence on the fraction of active motors (*39*). The chances any given bead will have more than one motor attached will be then be

$$P_2 = P(x > 1, C) = 1 - P(x = 0, C) - P(x = 1, C)$$

$$= 1 - \left(\frac{C_0 e^{-C}}{0!}\right) - \left(\frac{C_1 e^{-C}}{1!}\right) = 1 - e^{-C} - Ce^{-C} \qquad \text{Eq. 28}$$
$$= 1 - (1 + C)e^{-C}.$$

Thus, if two or more motors are needed to move a bead, the fraction *F* of moving beads as a function of the relative motor concentration *c* is

$$F_2(c) = P_2 = 1 - (1 + \lambda c)e^{-\lambda c}. \qquad \text{Eq. 29}$$

Assuming we are studying a (weakly) processive motor, we can finally estimate the motor concentration we should use to be sure that only one motor contributes to the observed force generation. The probability that a bead has more than one motor is $1 - (1 + C)e^{-C}$. We can re-write this in terms of *F* by noting that $F = 1 - e^{-C}$ for a processive motor, so $C = -\ln(1 - F)$. Thus:

$$\begin{aligned} P(x > 1) &= 1 - (1 - \ln(1 - F))e^{\ln(1-F)} \\ &= 1 - (1 - \ln(1 - F))(1 - F) \\ &= F + \ln(1 - F)\,(1 - F). \end{aligned} \qquad \text{Eq. 30}$$

To obtain a smaller than 5% probability of choosing a bead with more than one motor, we calculate

$$P(x > 1) = 0.05 = F + \ln(1 - F)(1 - F) \qquad \text{Eq. 31}$$

and solve for *F* numerically, which yields *F* = 0.299.

To finally determine the probability that only one motor interacts with a microtubule and contributes to force generation, we calculate the probability that two randomly attached dynein molecules are positioned close enough to one another that they could simultaneously bind to a microtubule. Assuming a random distribution of motors on the bead surface, the upper probability limit can be estimated by $(\pi dl/\pi d^2)^2 = (l/d)^2$, with *l* and *d* being the reach of the motor and the bead diameter, respectively. The reach of the full-length dynein molecule can be estimated from the putative length of the stalk and the diameter of the dynein head ring (~15 nm each (*86*)), the length of the detached linker element (~10 nm (*86*)), the approximate length of the tail domain (~30 nm (*87*)) and the size of the GFP and α-GFP antibody complex (~15 nm). The combined lengths result in a dynein reach of ~85 nm and together with an average bead diameter of 920 nm, this calculation yields an estimation of $p < 0.009$. Collectively, there is a >99.9996% probability that the observed movements are due to single dynein molecules at the dynein-bead ratios used. However, as we calculate the probability of two motors interacting with an infinite planar surface rather than a single linear microtubule of 25-nm diameter and as we assume a 100% probability that binding will take place simultaneously if it can take place (which is not the case), this proability is significantly underestimated.

Supplemental Figures and Table

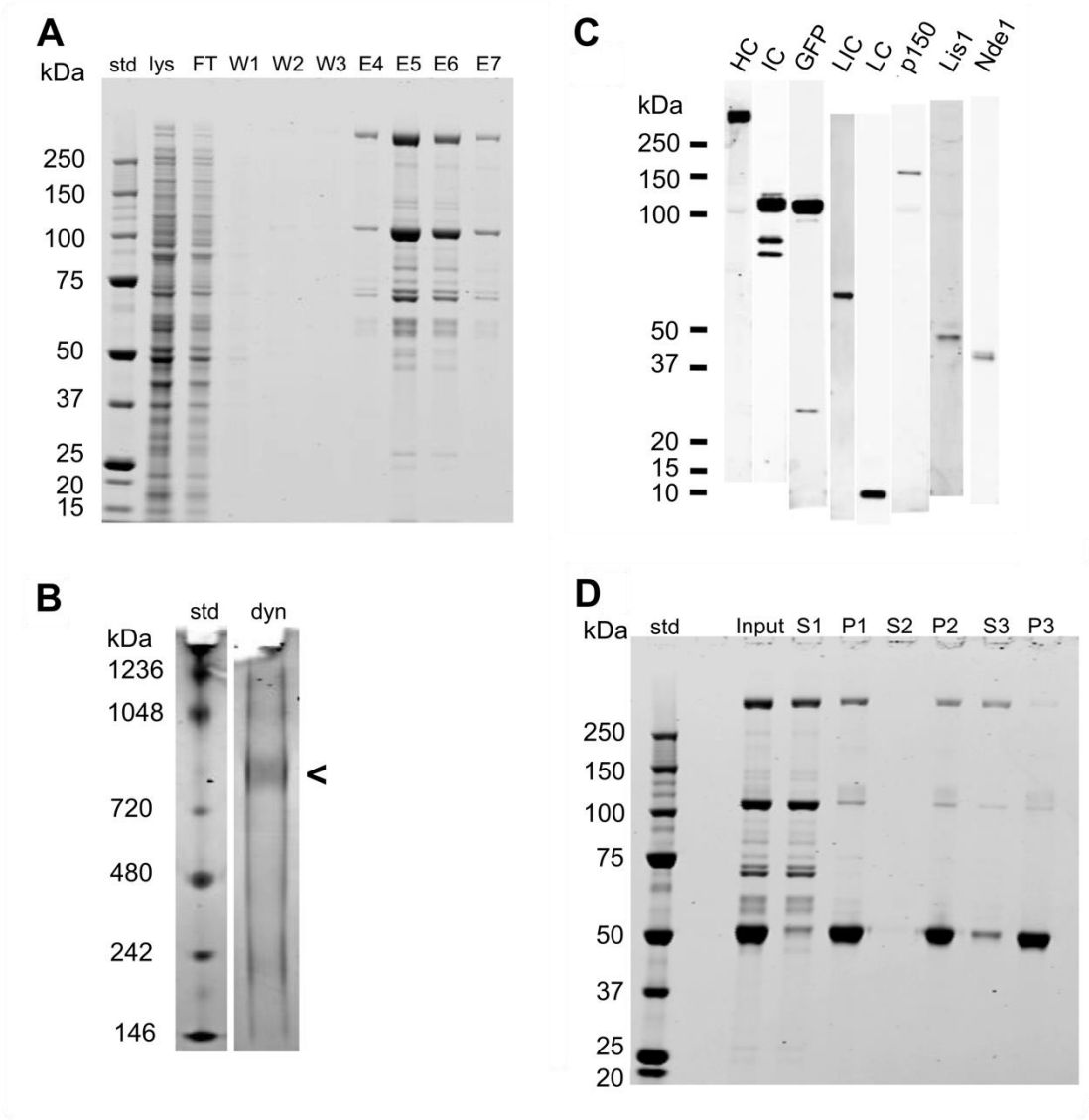

Fig. S1: Purification of human cytoplasmic dynein from HEK 293 cells and biochemical characterization.

(A) 4-12% Bis-Tris SDS-PAGE of StrepTrap HP purification, InstaBlue stain. Std., 10 µl precision plus protein standard (BioRad); lys, 0.5 µl cell lysate; FT, 0.5 µl StrepTrap column flow-through; W1, 0.5 µl of wash fraction 1; W2, 10 µl of wash fraction 2; W3, 10 ul of wash fraction 3; E4-E7, 10 µl of elution fractions 4 to 7. (B) Light blue native PAGE. 10 µl of StrepTrap-released dynein (dyn) was run on a 4-16% Bis-Tris gel according to the manufacturer's (Life Technologies) standard protocol using NativeMark protein standard (std., Life Technologies) and a standard silver stain procedure. Human cytoplasmic dynein is predominantly dimeric (arrowhead). (C) Western Blot analysis (see methods for details). 10 µl of StrepTrap-released dynein was run in each lane. HC, dynein heavy chain; IC, dynein intermediate chain; GFP, green fluorescent protein; LIC, dynein light intermediate chain; LC, dynein light chain; p150, dynactin p150 subunit; Lis1, lissencephaly protein 1; Nde1, nuclear distribution element 1. Please note that the relative intensities of the bands do not correlate with actual relative concentrations of the proteins due to different transfer conditions, transfer efficiencies, antibody reactivities, etc. (D) 4-12% Bis-Tris SDS-PAGE of MT-binding-release (see methods for details), InstaBlue stain. Std., as in (A); input, 5 µl of elution fraction 5 (panel A) supplemented with 20 µM tx, 1 mM AMPPNP, and 3 µM MTs; S1, 5 µl supernatant following UC spin; P1, 5 µl of re-suspended MT-pellet; S2, 5 µl of supernatant following a second UC spin; P2, 5 µl of MT-pellet re-suspended in 10 mM ATP containing buffer; S3, 5 µl of supernatant following the third UC spin, dynein-containing ATP-release fraction; P3, 5 µl of re-suspended MT-pellet following third UC spin.

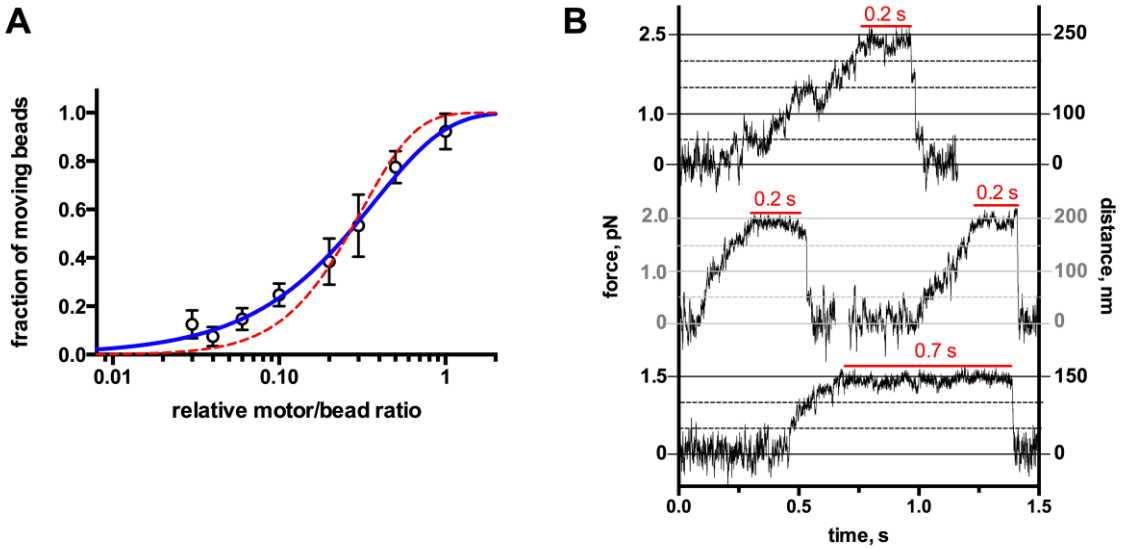

Fig. S2. Dilution curve for human cytoplasmic dynein bound non-specifically to carboxyl-beads using a trap stiffness of 0.01 pN/nm at saturating [ATP] and exemplary high force stall traces at 30% bead movement.

(A) Dilution curve counting beads as "moving", if forces equaled or exceeded 0.5 pN, equivalent to 50 nm, and if such a bead displacement was not reached via a single jump-like step (N_{total} = 318; 12-85 beads tested for each dilution). Error bars were calculated assuming a binomial distribution (error bar = ± sqrt ((1-f)*f/N), N = number of counted beads, f=fraction of moving beads); 12-85 beads were tested for each dilution (N_{total} = 318). Equations assuming one-or-more motors (blue solid line, R^2 = 0.9917, y = 1 – exp(-L*x), "processive" model) and two-or-more motors (red dashed line, R^2 = 0.9377, y=1 – exp(-L*x) – L*x*exp(-L*x), "non-processive" model) were fitted to the data points. To determine which of the two models fits best, we used Akaike's information criterion resulting in a 99.97% probability that the processive model is correct. See Figure 1 for the dilution curve counting jump-like behavior as movement. (B) Additional example stall traces yielding up to 2.4 pN at 1.1 mM ATP using a trap stiffness of 0.01 pN/nm at 30% bead movement (see Figure 1 for representative traces).

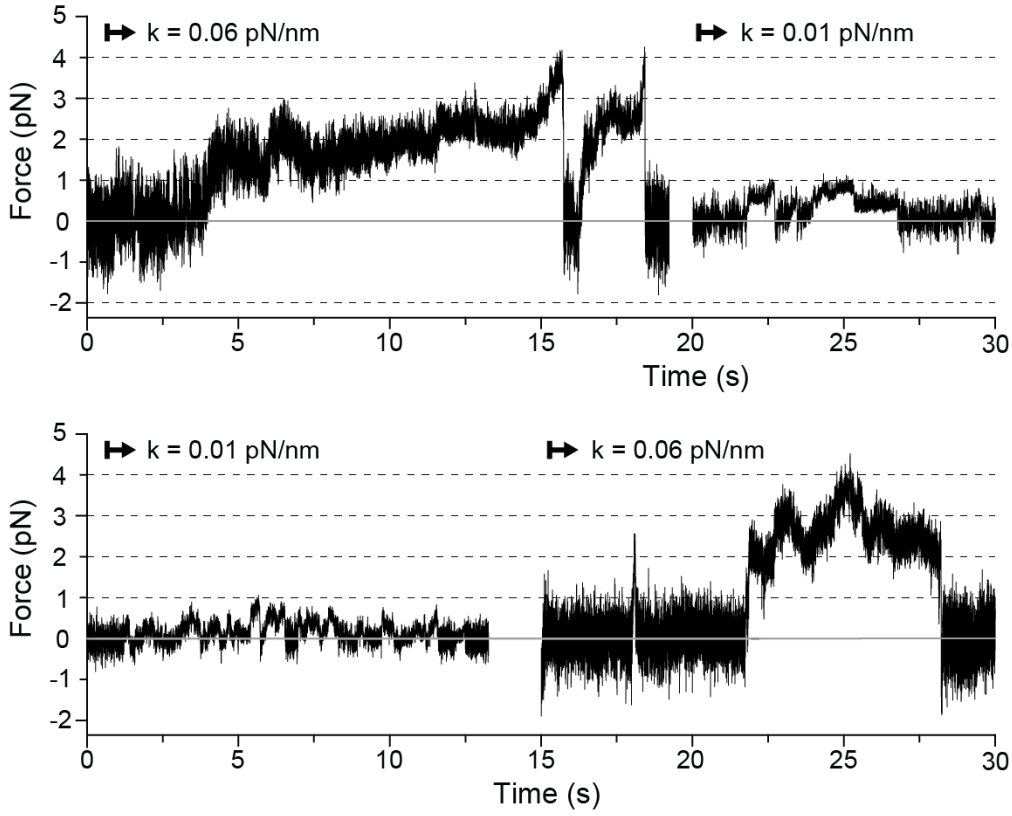

Fig. S3: Reversibility of the changes in the force generation of human cytoplasmic dynein with trap stiffness.

Example records showing force generation events of a single dynein molecule bound non-specifically to a trapping bead measured at 0.06 pN/nm (top left), 0.01 pN/nm (top right and bottom left) and again 0.06 pN/nm (bottom right), demonstrating the reversibility of the changes in force generation with changes in the trap stiffness.

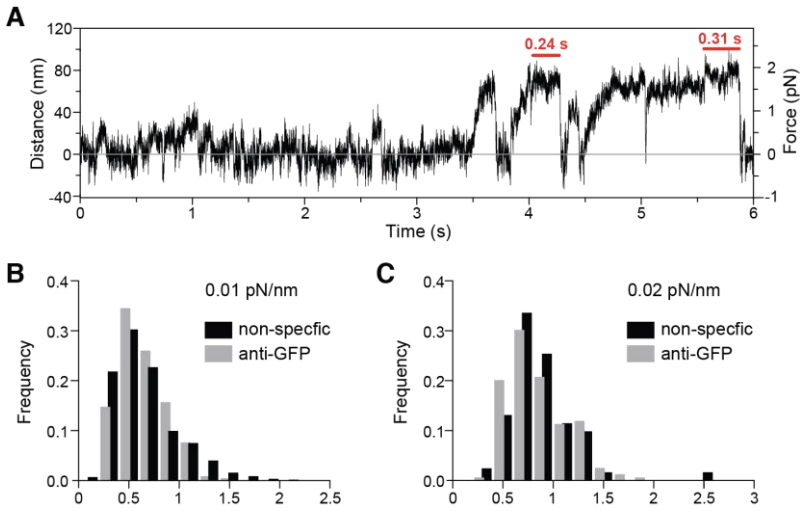

Fig. S4: Force generation of human cytoplasmic dynein bound specifically to an anti-GFP antibody coated polystyrene bead.

(A) Example trace segment showing force generation events of a single human dynein molecule bound specifically to a 0.9 μm diameter trapping bead via an anti-GFP antibody at 1.1 mM ATP and k = of 0.024 pN/nm. Stalling events (red horizontal bars) can be observed but are rare. (B) All measured forces ("detachment forces") acquired at k = 0.01 pN/nm at 1.1 mM ATP generated by dynein motors bound specifically to anti-GFP antibody coated beads (0.64 ± 0.02 pN, mean force ± SEM; shaded in grey; N = 233) and bound non-specifically to carboxyl-beads (0.64 ± 0.01 pN, mean force ± SEM; shaded in black; N = 572; reproduced from Fig. 2B of the main text for comparison). (C) Detachment forces acquired at k = 0.02 pN/nm at 1.1 mM ATP for dynein motors bound specifically (0.88 ± 0.03 pN; shaded in grey; N = 159) and bound non-specifically to beads (0.87 ± 0.03 pN, mean force ± SEM; N = 122).

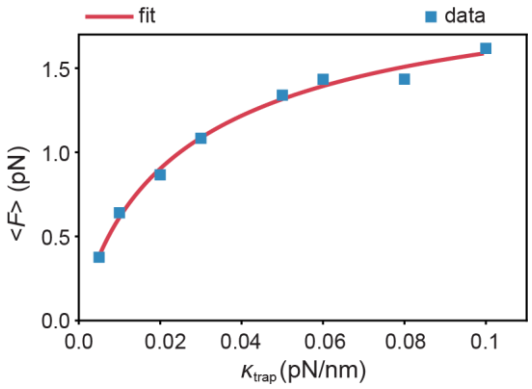

Fig. S5: Measured average detachment forces as a function of the trap stiffness k **analyzed with a model that assumes an exponentially increasing unbinding rate.**

Average detachment force as a function of trap stiffness. Fitting a model with an underlying exponentially force-dependent unbinding rate to the experimental data results in a stall force of $F_s = 2.1 \pm 0.2$ pN and a force-free run length $x_0 = 110 \pm 30$ nm.

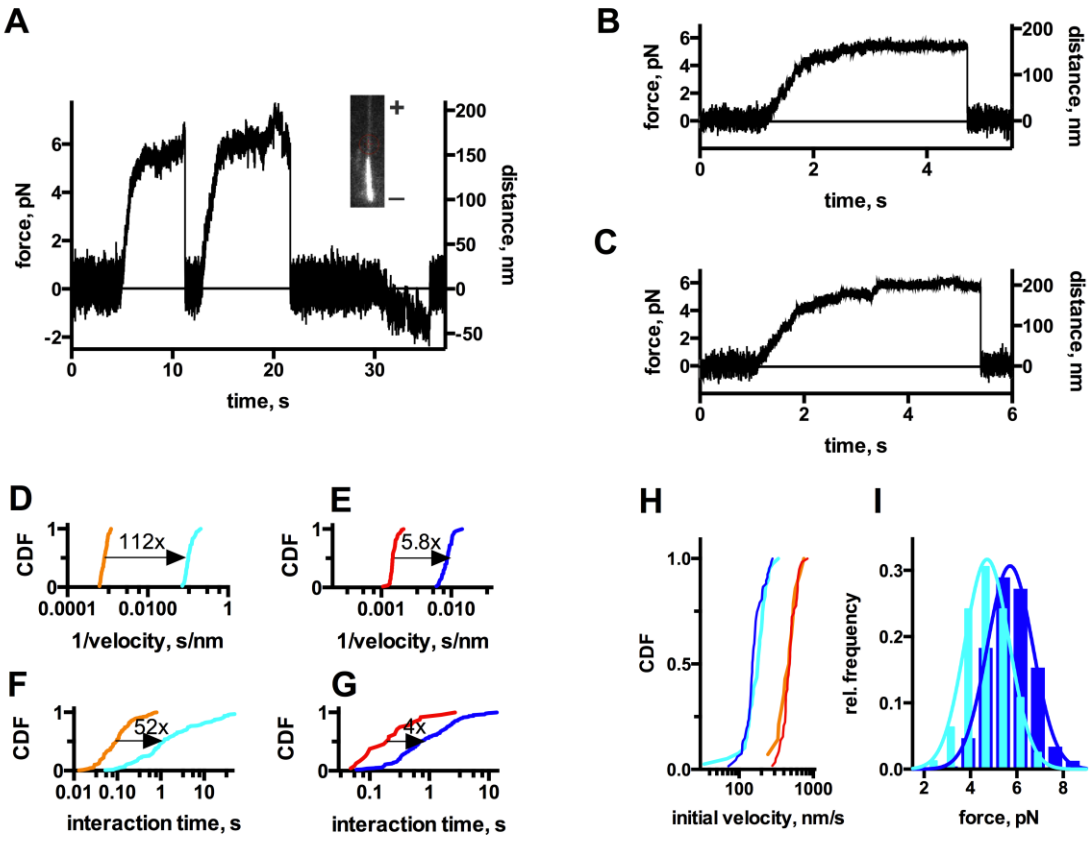

Fig. S6: Characterizing the bidirectional force generation of the human dynein StrepTrap release fraction.

All experiments were conducted in Pipes-Hepes buffer at RT. (A-C) Representative optical trapping traces (k ~ 0.03 pN/nm). The undiluted human dynein containing StrepTrap release fraction bound non-specifically to carboxyl-beads showed bidirectional force generation in the presence of 1 mM ATP (for bead statistics see Table S1). The inset in (A) depicts a polarity-marked MT used to judge directionality (minus end brightly labeled). The observed plus end-directed motion (B, 1 mM GTP) resembled force-generation events obtained with GFP-kinesin-1 (K560) bound to beads via anti-GFP antibodies (C, 1 mM GTP). (D, E) MT-gliding activity of StrepTrap release fraction (minus end-directed, D) in comparison with K560-kinesin (plus end-directed, E). Cumulative distribution functions (CDF) are displayed for the inverted MT-gliding velocities. Average inverted velocities of dynein-related minus end-directed motion were decreased 112-fold when using 1 mM GTP (cyan) as fuel compared to 1 mM ATP (orange), while the kinesin-driven plus end-directed motion was only affected by a factor of 5.8 (blue, red). (F, G) Interaction times of force generation events in the optical trap. Interaction times were defined as the time span between the start of the bead displacement and the return of the bead to the trap center. Cumulative distribution functions (CDF) are shown for bead displacements observed using ATP (orange, red) and GTP (cyan, blue) as fuel. Average interaction times of the minus end-directed motion were decreased 52-fold when using 1 mM GTP (cyan) as fuel instead of 1 mM ATP (orange), while the plus end-directed motion was only affected by a factor of 4 (blue, red). (H) CDFs of the plus end-directed bead displacement velocity. A linear equation was fitted to the initial, linear incline of the optical trapping traces with the velocities resulting from the slopes. Velocities of the plus end-directed "dynein" motion (1 mM ATP, orange; 1 mM GTP, cyan) were compared to velocities of K560-kinesin (1 mM ATP, red; 1 mM GTP, blue). (I) Stall force histograms obtained from the plus end-directed motion of the StrepTrap release (cyan) and GFP-kinesin (blue) at 1 mM GTP using a trap stiffness of 0.06 pN/nm (F_{stall} = 4.8 ± 0.9 pN (N = 157) and 5.8 ± 0.9 pN (N = 235), respectively; ± SD). Solid lines are approximations by a Gaussian distribution function.

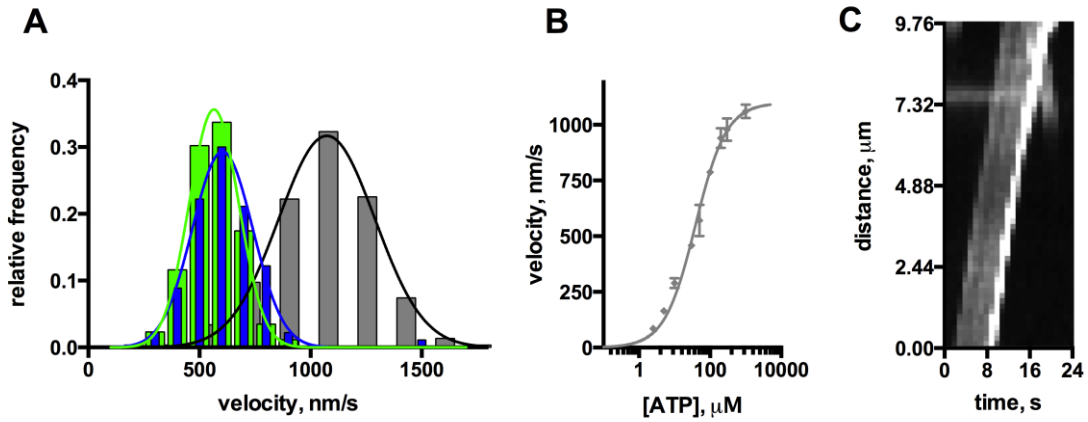

Fig. S7: MT-gliding activity of human cytoplasmic dynein. The MT-gliding activity of the dynein StrepTrap release fraction was analyzed in Pipes-Hepes gliding buffer at RT using TRITC-labeled MTs in a TIRF microscope assay.

(A) Velocity histograms of dynein bound non-specifically (NS) to HCl-EtOH-cleaned coverslips (gray), attached via intermediate chain (IC) antibody (MAB1618, green), and via heavy chain (HC) antibody (blue). Solid lines are Gaussian fits yielding the following mean values (± SEM): v (IC) = 565 ± 1 nm/s (R^2 = 0.9994, N = 88), v (HC) = 604 ± 3 nm/s (R^2 = 0.9994, N = 90), and v (NS) = 1073 ± 6 nm/s (R^2 = 0.9956, N = 285). (B) ATP-concentration dependence of MT-gliding velocity for non-specifically bound dynein. Average velocities ± 2 SEM from two independent experiments using two different dynein purifications. Solid line represents hyperbolic fit ($v = v_{max}$*[ATP]/(K_M+[ATP])) yielding a maximum velocity of 1100 ± 30 nm/s and a Michaelis-Menten constant K_M (69) of 39 ± 4 µM. (C) Kymograph of a polarity-marked MT (minus end brightly labeled) generated by marking the MT-track in a tif image stack in ImageJ and re-slicing the selected track over time. Since dynein is bound to the coverslip performing minus end-directed power strokes, the dimly labeled MT plus end is being pushed forward and the bright minus end constitutes the trailing MT end. 70/70 tested polarity-marked MTs moved with the bright end trailing, i.e. 100% of the movement was minus end-directed. In the kymograph, the same distance position is reached first by the dim MT plus end and at a later time point by the bright minus end.

Table S1: Characterization of the plus end-directed motion of human dynein StrepTrap release and comparison with kinesin-1 (K560).

Experiments were performed in Pipes-Hepes buffer at RT (see Fig. S6). (A) Bead statistics of plus- and minus end-directed motion observed for StrepTrap release fraction in the presence of 1 mM ATP and 1 mM GTP, respectively. (B). Initial velocities of force generation events in the optical trap for K560-kinesin and the plus end-directed motion in the StrepTrap release. (C). Interaction times of force generation events of the plus and minus end-directed motion observed with StrepTrap release. Interaction times were defined as the time span between the start of the bead displacement and the return of the bead to the trap center. (D). MT-gliding velocities of K560-kinesin and human dynein-containing StrepTrap release at 1 mM ATP and 1 mM GTP.

(A). Bead statistics		
% of beads that show	**1 mM ATP**	**1 mM GTP**
Minus end motion	70	46
Plus end motion	30	29
Plus-minus end motion	30	17
Binding w/o movement	0	42
Rigor binding	0	21
nothing	30	0
(B). Initial velocities of force generation events in the optical trap		
	1 mM ATP velocity ± SEM, nm/s	**1 mM GTP** velocity ± SEM, nm/s
K560 plus end motion	488 ± 14	162 ± 6
StrepTrap release plus end motion	473 ± 36	173 ± 7
(C). Average interaction times of force generation events in StrepTrap release		
	1 mM ATP interaction time ± SEM, s	**1 mM GTP** interaction time ± SEM, s
Plus end-directed force generation	0.4 ± 0.1	1.6 ± 0.2
Minus end-directed force generation	0.14 ± 0.01	7.3 ± 1.4
(D). MT-gliding velocities		
	1 mM ATP velocity ± SEM, nm/s	**1 mM GTP** velocity ± SEM, nm/s
K560 MT-gliding (plus end-directed)	674 ± 11	116 ± 3
Human dynein MT-gliding (minus end-directed)	1060 ± 30	9.5 ± 0.3

REFERENCES AND NOTES

1. J. R. Kardon, R. D. Vale, Regulators of the cytoplasmic dynein motor. *Nat. Rev. Mol. Cell Biol.* **10**, 854–865 (2009).

2. S. R. White, B. Lauring, AAA+ ATPases: Achieving diversity of function with conserved machinery. *Traffic* **8**, 1657–1667 (2007).

3. M. A. Olenick, E. L. F. Holzbaur, Dynein activators and adaptors at a glance. *J. Cell Sci.* **132**, jcs227132 (2019).

4. J. K. Moore, J. A. Cooper, Coordinating mitosis with cell polarity: Molecular motors at the cell cortex. *Semin. Cell Dev. Biol.* **21**, 283–289 (2010).

5. J. R. Bader, K. T. Vaughan, Dynein at the kinetochore: Timing, interactions and functions. *Semin. Cell Dev. Biol.* **21**, 269–275 (2010).

6. R. B. Vallee, G. E. Seale, J.-W. Tsai, Emerging roles for myosin II and cytoplasmic dynein in migrating neurons and growth cones. *Trends Cell Biol.* **19**, 347–355 (2009).

7. K. Zhang, H. E. Foster, A. Rondelet, S. E. Lacey, N. Bahi-Buisson, A. W. Bird, A. P. Carter, Cryo-EM reveals how human cytoplasmic dynein is auto-inhibited and activated. *Cell* **169**, 1303–1314.e18 (2017).

8. S. L. Reck-Peterson, A. Yildiz, A. P. Carter, A. Gennerich, N. Zhang, R. D. Vale, Single-molecule analysis of dynein processivity and stepping behavior. *Cell* **126**, 335–348 (2006).

9. M. Nishiura, T. Kon, K. Shiroguchi, R. Ohkura, T. Shima, Y. Y. Toyoshima, K. Sutoh, A single-headed recombinant fragment of *Dictyostelium* cytoplasmic dynein can drive the robust sliding of microtubules. *J. Biol. Chem.* **279**, 22799–22802 (2004).

10. M. P. Nicholas, P. Höök, S. Brenner, C. L. Wynne, R. B. Vallee, A. Gennerich, Control of cytoplasmic dynein force production and processivity by its C-terminal domain. *Nat. Commun.* **6**, 6206 (2015).

11. C. Cho, S. L. Reck-Peterson, R. D. Vale, Regulatory ATPase sites of cytoplasmic dynein affect processivity and force generation. *J. Biol. Chem.* **283**, 25839–25845 (2008).

12. V. Belyy, M. A. Schlager, H. Foster, A. E. Reimer, A. P. Carter, A. Yildiz, The mammalian dynein–dynactin complex is a strong opponent to kinesin in a tug-of-war competition. *Nat. Cell Biol.* **18**, 1018–1024 (2016).

13. L. Rao, M. Hülsemann, A. Gennerich, Combining structure–function and single-molecule studies on cytoplasmic dynein. *Methods Mol. Biol.* **1665**, 53–89 (2018).

14. A. Gennerich, A. P. Carter, S. L. Reck-Peterson, R. D. Vale, Force-induced bidirectional stepping of cytoplasmic dynein. *Cell* **131**, 952–965 (2007).

15. B. H. Blehm, P. R. Selvin, Single-molecule fluorescence and in vivo optical traps: How multiple dyneins and kinesins interact. *Chem. Rev.* **114**, 3335–3352 (2014).

16. W. J. Walter, B. Brenner, W. Steffen, Cytoplasmic dynein is not a conventional processive motor. *J. Struct. Biol.* **170**, 266–269 (2010).

17. K. M. Ori-McKenney, J. Xu, S. P. Gross, R. B. Vallee, A cytoplasmic dynein tail mutation impairs motor processivity. *Nat. Cell Biol.* **12**, 1228–1234 (2010).

18. A. K. Rai, A. Rai, A. J. Ramaiya, R. Jha, R. Mallik, Molecular adaptations allow dynein to generate large collective forces inside cells. *Cell* **152**, 172–182 (2013).

19. S. Toba, T. M. Watanabe, L. Yamaguchi-Okimoto, Y. Y. Toyoshima, H. Higuchi, Overlapping hand-over-hand mechanism of single molecular motility of cytoplasmic dynein. *Proc. Natl. Acad. Sci. U.S.A.* **103**, 5741–5745 (2006).

20. R. Mallik, D. Petrov, S. A. Lex, S. J. King, S. P. Gross, Building complexity: An in vitro study of cytoplasmic dynein with in vivo implications. *Curr. Biol.* **15**, 2075–2085 (2005).

21. R. Mallik, B. C. Carter, S. A. Lex, S. J. King, S. P. Gross, Cytoplasmic dynein functions as a gear in response to load. *Nature* **427**, 649–652 (2004).

22. M. Trokter, N. Mücke, T. Surrey, Reconstitution of the human cytoplasmic dynein complex. *Proc. Natl. Acad. Sci. U.S.A.* **109**, 20895–20900 (2012).

23. M. Miura, A. Matsubara, T. Kobayashi, M. Edamatsu, Y. Y. Toyoshima, Nucleotide-dependent behavior of single molecules of cytoplasmic dynein on microtubules in vitro. *FEBS Lett.* **584**, 2351–2355 (2010).

24. S. J. King, T. A. Schroer, Dynactin increases the processivity of the cytoplasmic dynein motor. *Nat. Cell Biol.* **2**, 20–24 (2000).

25. J. L. Ross, K. Wallace, H. Shuman, Y. E. Goldman, E. L. Holzbaur, Processive bidirectional motion of dynein–Dynactin complexes in vitro. *Nat. Cell Biol.* **8**, 562–570 (2006).

26. T. Torisawa, M. Ichikawa, A. Furuta, K. Saito, K. Oiwa, H. Kojima, Y. Y. Toyoshima, K. Furuta, Autoinhibition and cooperative activation mechanisms of cytoplasmic dynein. *Nat. Cell Biol.* **16**, 1118–1124 (2014).

27. D. J.-K. Hu, A. D. Baffet, T. Nayak, A. Akhmanova, V. Doye, R. B. Vallee, Dynein recruitment to nuclear pores activates apical nuclear migration and mitotic entry in brain progenitor cells. *Cell* **154**, 1300–1313 (2013).

28. S. C. Tan, J. Scherer, R. B. Vallee, Recruitment of dynein to late endosomes and lysosomes through light intermediate chains. *Mol. Biol. Cell* **15**, 467–477 (2010).

29. M. van Spronsen, M. Mikhaylova, J. Lipka, M. A. Schlager, D. J. van den Heuvel, M. Kuijpers, P. S. Wulf, N. Keijzer, J. Demmers, L. C. Kapitein, D. Jaarsma, H. C. Gerritsen, A. Akhmanova, C. C. Hoogenraad, TRAK/Milton motor-adaptor proteins steer mitochondrial trafficking to axons and dendrites. *Neuron* **77**, 485–502 (2013).

30. M. A. Schlager, H. T. Hoang, L. Urnavicius, S. L. Bullock, A. P. Carter, In vitro reconstitution of a highly processive recombinant human dynein complex. *EMBO J.* **33**, 1855–1868 (2014).

31. R. J. McKenney, W. Huynh, M. E. Tanenbaum, G. Bhabha, R. D. Vale, Activation of cytoplasmic dynein motility by dynactin-cargo adapter complexes. *Science* **345**, 337–341 (2014).

32. L. A. Amos, Brain dynein crossbridges microtubules into bundles. *J. Cell Sci.* **93**, 19–28 (1989).

33. M. A. Olenick, M. Tokito, M. Boczkowska, R. Dominguez, E. L. Holzbaur, Hook adaptors induce unidirectional processive motility by enhancing the dynein-dynactin interaction. *J. Biol. Chem.* **291**, 18239–18251 (2016).

34. M. M. Elshenawy, J. T. Canty, L. Oster, L. S. Ferro, Z. Zhou, S. C. Blanchard, A. Yildiz, Cargo adaptors regulate stepping and force generation of mammalian dynein-dynactin. *Nat. Chem. Biol.* **15**, 1093–1101 (2019).

35. M. Ichikawa, Y. Watanabe, T. Murayama, Y. Y. Toyoshima, Recombinant human cytoplasmic dynein heavy chain 1 and 2: Observation of dynein-2 motor activity in vitro. *FEBS Lett.* **585**, 2419–2423 (2011).

36. T. L. Culver-Hanlon, S. A. Lex, A. D. Stephens, N. J. Quintyne, S. J. King, A microtubule-binding domain in dynactin increases dynein processivity by skating along microtubules. *Nat. Cell Biol.* **8**, 264–270 (2006).

37. T. Kobayashi, N. Morone, T. Kashiyama, H. Oyamada, N. Kurebayashi, T. Murayama, Engineering a novel multifunctional green fluorescent protein tag for a wide variety of protein research. *PLOS ONE* **3**, e3822 (2008).

38. T. Kobayashi, T. Murayama, Cell cycle-dependent microtubule-based dynamic transport of cytoplasmic dynein in mammalian cells. *PLOS ONE* **4**, e7827 (2009).

39. K. Svoboda, S. M. Block, Force and velocity measured for single kinesin molecules. *Cell* **77**, 773–784 (1994).

40. K. Svoboda, C. F. Schmidt, B. J. Schnapp, S. M. Block, Direct observation of kinesin stepping by optical trapping interferometry. *Nature* **365**, 721–727 (1993).

41. S. M. Block, L. S. Goldstein, B. J. Schnapp, Bead movement by single kinesin molecules studied with optical tweezers. *Nature* **348**, 348–352 (1990).

42. W. R. Hesse, M. Steiner, M. L. Wohlever, R. D. Kamm, W. Hwang, M. J. Lang, Modular aspects of kinesin force generation machinery. *Biophys. J.* **104**, 1969–1978 (2013).

43. F. Berger, S. Klumpp, R. Lipowsky, Force-dependent unbinding rate of molecular motors from stationary optical trap data. *Nano Lett.* **19**, 2598–2602 (2019).

44. G. Bhabha, G. T. Johnson, C. M. Schroeder, R. D. Vale, How dynein moves along microtubules. *Trends Biochem. Sci.* **41**, 94–105 (2016).

45. L. Rao, F. Berger, M. P. Nicholas, A. Gennerich, Molecular mechanism of cytoplasmic dynein tension sensing. *Nat. Commun.* **10**, 3332 (2019).

46. T. Bameta, R. Padinhateeri, M. M. Inamdar, Force generation and step-size fluctuations in a dynein motor. *J. Stat. Mech. Theory Exp.* **2013**, P02030 (2013).

47. J. R. Kardon, S. L. Reck-Peterson, R. D. Vale, Regulation of the processivity and intracellular localization of *Saccharomyces cerevisiae* dynein by dynactin. *Proc. Natl. Acad. Sci. U.S.A.* **106**, 5669–5674 (2009).

48. G. Woehlke, A. K. Ruby, C. L. Hart, B. Ly, N. Hom-Booher, R. D. Vale, Microtubule interaction site of the kinesin motor. *Cell* **90**, 207–216 (1997).

49. L. Romberg, D. W. Pierce, R. D. Vale, Role of the kinesin neck region in processive microtubule-based motility. *J. Cell Biol.* **140**, 1407–1416 (1998).

50. K. S. Thorn, J. A. Ubersax, R. D. Vale, Engineering the processive run length of the kinesin motor. *J. Cell Biol.* **151**, 1093–1100 (2000).

51. D. S. Friedman, R. D. Vale, Single-molecule analysis of kinesin motility reveals regulation by the cargo-binding tail domain. *Nat. Cell Biol.* **1**, 293–297 (1999).

52. H. W. Schroeder III, A. G. Hendricks, K. Ikeda, H. Shuman, V. Rodionov, M. Ikebe, Y. E. Goldman, E. L. Holzbaur, Force-dependent detachment of kinesin-2 biases track switching at cytoskeletal filament intersections. *Biophys. J.* **103**, 48–58 (2012).

53. H. Yardimci, M. van Duffelen, Y. Mao, S. S. Rosenfeld, P. R. Selvin, The mitotic kinesin CENP-E is a processive transport motor. *Proc. Natl. Acad. Sci. U.S.A.* **105**, 6016–6021 (2008).

54. C. M. Coppin, D. W. Pierce, L. Hsu, R. D. Vale, The load dependence of kinesin's mechanical cycle. *Proc. Natl. Acad. Sci. U.S.A.* **94**, 8539–8544 (1997).

55. K. Furuta, A. Furuta, Y. Y. Toyoshima, M. Amino, K. Oiwa, H. Kojima, Measuring collective transport by defined numbers of processive and nonprocessive kinesin motors. *Proc. Natl. Acad. Sci. U.S.A.* **110**, 501–506 (2013).

56. K. Visscher, M. J. Schnitzer, S. M. Block, Single kinesin molecules studied with a molecular force clamp. *Nature* **400**, 184–189 (1999).

57. S. Pyrpassopoulos, H. Shuman, E. M. Ostap, Modulation of kinesin's load-bearing capacity by force geometry and the microtubule track. *Biophys. J.* **118**, 243–253 (2020).

58. M. J. Korneev, S. Lakämper, C. F. Schmidt, Load-dependent release limits the processive stepping of the tetrameric Eg5 motor. *Eur. Biophys. J.* **36**, 675–681 (2007).

59. M. P. Nicholas, L. Rao, A. Gennerich, An improved optical tweezers assay for measuring the force generation of single Kinesin molecules. *Methods Mol. Biol.* **1136**, 171–246 (2014).

60. M. P. Nicholas, L. Rao, A. Gennerich, Covalent immobilization of microtubules on glass surfaces for molecular motor force measurements and other single-molecule assays. *Methods Mol. Biol.* **1136**, 137–169 (2014).

61. E. Schäffer, S. F. Nørrelykke, J. Howard, Surface forces and drag coefficients of microspheres near a plane surface measured with optical tweezers. *Langmuir* **23**, 3654–3665 (2007).

62. P. Romac, T. Žanić-Grubisić, O. Ćulić, P. Cvitković, M. Flogel, Sperm motility and kinetics of dynein ATPase in astheno- and normozoospermic samples after stimulation with adenosine and its analogues. *Hum. Reprod.* **9**, 1474–1478 (1994).

63. R. B. Case, D. W. Pierce, N. Hom-Booher, C. L. Hart, R. D. Vale, The directional preference of kinesin motors is specified by an element outside of the motor catalytic domain. *Cell* **90**, 959–966 (1997).

64. J. Howard, A. A. Hyman, Preparation of marked microtubules for the assay of the polarity of microtubule-based motors by fluorescence microscopy. *Methods Cell Biol.* **39**, 105–113 (1993).

65. R. D. Vale, Y. Y. Toyoshima, Rotation and translocation of microtubules in vitro induced by dyneins from *Tetrahymena* cilia. *Cell* **52**, 459–469 (1988).

66. A. Edelstein, N. Amodaj, K. Hoover, R. Vale, N. Stuurman, Computer control of microscopes using μManager. *Curr. Protoc. Mol. Biol.* **92**, Unit14.20 (2010).

67. E. Meijering, O. Dzyubachyk, I. Smal, Methods for cell and particle tracking. *Methods Enzymol.* **504**, 183–200 (2012).

68. M. Swoboda, J. Henig, H.-M. Cheng, D. Brugger, D. Haltrich, N. Plumeré, M. Schlierf, Enzymatic oxygen scavenging for photostability without pH drop in single-molecule experiments. *ACS Nano* **6**, 6364–6369 (2012).

69. P. Satpute-Krishnan, J. A. DeGiorgis, M. P. Conley, M. Jang, E. L. Bearer, A peptide zipcode sufficient for anterograde transport within amyloid precursor protein. *Proc. Natl. Acad. Sci. U.S.A.* **103**, 16532–16537 (2006).

70. T. Shimizu, Y. Y. Toyoshima, M. Edamatsu, R. D. Vale, Comparison of the motile and enzymatic properties of two microtubule minus-end-directed motors, ncd and cytoplasmic dynein. *Biochemistry* **34**, 1575–1582 (1995).

71. H. S. Shpetner, B. M. Paschal, R. B. Vallee, Characterization of the microtubule-activated ATPase of brain cytoplasmic dynein (MAP 1C). *J. Cell Biol.* **107**, 1001–1009 (1988).

72. J. Roostalu, C. Hentrich, P. Bieling, I. A. Telley, E. Schiebel, T. Surrey, Directional switching of the kinesin Cin8 through motor coupling. *Science* **332**, 94–99 (2011).

73. H. Kojima, E. Muto, H. Higuchi, T. Yanagida, Mechanics of single kinesin molecules measured by optical trapping nanometry. *Biophys. J.* **73**, 2012–2022 (1997).

74. L. A. Ligon, M. Tokito, J. M. Finklestein, F. E. Grossman, E. L. F. Holzbaur, A direct interaction between cytoplasmic dynein and kinesin I may coordinate motor activity. *J. Biol. Chem.* **279**, 19201–19208 (2004).

75. A. J. Firestone, J. S. Weinger, M. Maldonado, K. Barlan, L. D. Langston, M. O'Donnell, V. I. Gelfand, T. M. Kapoor, J. K. Chen, Small-molecule inhibitors of the AAA+ ATPase motor cytoplasmic dynein. *Nature* **484**, 125–129 (2012).

76. B. M. Paschal, H. S. Shpetner, R. B. Vallee, MAP 1C is a microtubule-activated ATPase which translocates microtubules in vitro and has dynein-like properties. *J. Cell Biol.* **105**, 1273–1282 (1987).

77. S. C. Kuo, M. P. Sheetz, Force of single kinesin molecules measured with optical tweezers. *Science* **260**, 232–234 (1993).

78. V. Belyy, N. L. Hendel, A. Chien, A. Yildiz, Cytoplasmic dynein transports cargos via load-sharing between the heads. *Nat. Commun.* **5**, 5544 (2014).

79. W. P. Wong, K. Halvorsen, The effect of integration time on fluctuation measurements: Calibrating an optical trap in the presence of motion blur. *Opt. Express* **14**, 12517–12531 (2006).

80. M. P. Nicholas, F. Berger, L. Rao, S. Brenner, C. Cho, A. Gennerich, Cytoplasmic dynein regulates its attachment to microtubules via nucleotide state-switched mechanosensing at multiple AAA domains. *Proc. Natl. Acad. Sci. U.S.A.* **112**, 6371–6376 (2015).

81. O. K. Dudko, G. Hummer, A. Szabo, Intrinsic rates and activation free energies from single-molecule pulling experiments. *Phys. Rev. Lett.* **96**, 108101 (2006).

82. O. K. Dudko, G. Hummer, A. Szabo, Theory, analysis, and interpretation of single-molecule force spectroscopy experiments. *Proc. Natl. Acad. Sci. U.S.A.* **105**, 15755–15760 (2008).

83. G. I. Bell, Models for the specific adhesion of cells to cells. *Science* **200**, 618–627 (1978).

84. S. Klumpp, C. Keller, F. Berger, R. Lipowsky, Molecular motors: Cooperative phenomena of multiple molecular motors, in *Multiscale Modeling in Biomechanics and Mechanobiology* (Springer, London, 2014), vol. 8.

85. A. Kunwar, S. K. Tripathy, J. Xu, M. K. Mattson, P. Anand, R. Sigua, M. Vershinin, R. J. McKenney, C. C. Yu, A. Mogilner, S. P. Gross, Mechanical stochastic tug-of-war models cannot explain bidirectional lipid-droplet transport. *Proc. Natl. Acad. Sci. U.S.A.* **108**, 18960–18965 (2011).

86. S. A. Burgess, M. L. Walker, H. Sakakibara, P. J. Knight, K. Oiwa, Dynein structure and power stroke. *Nature* **421**, 715–718 (2003).

87. J. Fan, L. A. Amos, Antibodies to cytoplasmic dynein heavy chain map the surface and inhibit motility. *J. Mol. Biol.* **307**, 1317–1327 (2001).